Signal Processing Systems
Mekelweg 4,
2628 CD Delft
The Netherlands
https://sps.ewi.tudelft.nl/

SPS-2025-5956560

M.Sc. Thesis

DoA Estimation for Arrays with Phase Incoherencies

Shipeng Liu

Abstract

Automotive radar is an important sensor technology for self-driving cars and Advanced Driver-Assistance Systems (ADAS). Current automotive radars lack the ability to classify and categorize objects due to their limited angular resolution. A new generation of automotive radar systems, known as automotive imaging radars, proposes to overcome this limitation by using larger apertures with more antenna elements. During the radar operation, automotive imaging radar systems face challenges in the accurate estimation of the Direction-of-Arrival (DoA) due to phase incoherency in the spatially sampled information caused by hardware imperfections, temperature variations, and aging effects. This work proposes a method combining convex optimization and alternating updates to first jointly calibrate the phase incoherencies and estimate the DoAs, and then update them iteratively. It further derives the Cramér-Rao Bound (CRB) and investigates the impact of the phase incoherency on DoA estimation using the CRB. In the proposed approach, the MUltiple SIgnal Classification (MUSIC) algorithm is applied to estimate the DoAs after each calibration. Additionally, the eigenvalue decomposition process in MUSIC is replaced by the Projection Approximation Subspace Tracking (PAST) algorithm to reduce computational complexity while maintaining the accuracy of DoA estimation. Experimental results illustrate the effectiveness of these techniques, highlighting their potential in improving next-generation automotive radar systems.

Faculty of Electrical Engineering, Mathematics and Computer Science
Delft University of Technology

DoA Estimation for Arrays with Phase Incoherencies

THESIS

submitted in partial fulfillment of the
requirements for the degree of

MASTER OF SCIENCE

in

ELECTRICAL ENGINEERING

by

Shipeng Liu
born in Shandong, China

This work was performed in:

Signal Processing Systems Group
Department of Microelectronics
Faculty of Electrical Engineering, Mathematics and Computer Science
Delft University of Technology

Delft University of Technology

Copyright © 2025 Signal Processing Systems Group
All rights reserved.

Delft University of Technology
Department of
Microelectronics

The undersigned hereby certify that they have read and recommend to the Faculty of Electrical Engineering, Mathematics and Computer Science for acceptance a thesis entitled **"DoA Estimation for Arrays with Phase Incoherencies"** by **Shipeng Liu** in partial fulfillment of the requirements for the degree of **Master of Science**.

Dated: 26th May 2025

Chairman:

prof.dr.ir. Geert Leus

Advisor:

prof.dr.ir. Geert Leus

Committee Members:

dr. Francesco Fioranelli

ir. Arie Koppelaar

Abstract

Automotive radar is an important sensor technology for self-driving cars and Advanced Driver-Assistance Systems (ADAS). Current automotive radars lack the ability to classify and categorize objects due to their limited angular resolution. A new generation of automotive radar systems, known as automotive imaging radars, proposes to overcome this limitation by using larger apertures with more antenna elements. During the radar operation, automotive imaging radar systems face challenges in the accurate estimation of the Direction-of-Arrival (DoA) due to phase incoherency in the spatially sampled information caused by hardware imperfections, temperature variations, and aging effects. This work proposes a method combining convex optimization and alternating updates to first jointly calibrate the phase incoherencies and estimate the DoAs, and then update them iteratively. It further derives the Cramér-Rao Bound (CRB) and investigates the impact of the phase incoherency on DoA estimation using the CRB. In the proposed approach, the MUltiple SIgnal Classification (MUSIC) algorithm is applied to estimate the DoAs after each calibration. Additionally, the eigenvalue decomposition process in MUSIC is replaced by the Projection Approximation Subspace Tracking (PAST) algorithm to reduce computational complexity while maintaining the accuracy of DoA estimation. Experimental results illustrate the effectiveness of these techniques, highlighting their potential in improving next-generation automotive radar systems.

Acknowledgments

I would like to thank my supervisors, Arie Koppelaar and Juan Osorio, from NXP Semiconductors Netherlands B.V.. During this thesis, they were always enthusiastic to share knowledge and have a discussion, whether it was in the meeting room or the coffee corner. Without their passion and insights, this thesis topic and the following work would not have been possible. More importantly, they introduced to me the engineering perspective.

I would also like to thank my advisor prof.dr.ir. Geert Leus for introducing me to this field and his assistance during this thesis. The entire work in this thesis is inseparable from his profound knowledge. Even before our very first discussion, I was impressed by Prof. Geert's teaching style in the course Statistical Digital Signal Processing and Modeling: rigorous and clear mathematical reasoning. That was also when I realized what I might be good at and where my interest lies. Applied Convex Optimisation, another course that Prof. Geert teaches, directly benefits the work in this thesis. Array Processing, again a course that he teaches, is the foundation required for this thesis topic. It was after that amazing oral exam for this course with Prof. Geert that I came to realize the complete picture of this course and, most importantly, the awareness that even in the knowledge I believed I had mastered, there is always more to discover. Since then, I became fully certain of my passion for this field.

Shipeng Liu
Delft, The Netherlands
26th May 2025

Contents

List of Figures

List of Tables

Nomenclature

$(\cdot)^T$	Transpose
$(\cdot)^H$	Hermitian
$\bar{(\cdot)}$	Complex conjugate of a vector or matrix
$(\cdot)^*$	Complex conjugate of a scalar
$\circ$	Khatri–Rao product
$\odot$	Element-wise product
$\otimes$	Kronecker product
$\circledast$	Convolution
$\mathrm{tr}(\cdot)$	Trace of a matrix
$\mathrm{diag}(\mathbf{x})$	Use the vector $\mathbf{x}$ to form a diagonal matrix
$\mathrm{diag}(\mathbf{X})$	Use the elements on the diagonal of the matrix $\mathbf{X}$ to form a vector
$\mathbf{1}_m$	All-one vector of size $m \times 1$
$\mathbf{0}_m$	All-zero vector of size $m \times 1$
$\mathbf{I}_m$	Identity matrix of size $m \times m$

Background

1

1.1 Introduction

Estimating the Direction-of-Arrival (DoA) of multiple far-field sources impinging on a spatially distributed antenna array is one of the key interests of radar systems, and angular resolution is one of the key performance indicators for DoA estimation. The angular resolution of the array is largely determined by its aperture, whereas the array's element density helps to enhance suppression outside the main lobe and mitigates spatial aliasing. A new generation of automotive radar systems, known as automotive imaging radars, therefore proposes to use larger apertures with more antenna elements.

In imaging radar systems, the transmitting and receiving radars have been traditionally built by cascading several radar integrated circuits (ICs), and the digitized output of all the receiving antennas is processed centrally in a single processor. Each IC can carry several transmitting or receiving entities, and these entities are referred to as transmitter or receiver dies. This modular approach reduces the cost of developing several ICs for diverse applications but increases the presence of model errors, primarily stemming from relative gain and phase mismatches between the antennas in the array. These gain and phase mismatches between antennas are referred to as gain and phase errors. In general, the gain errors can be mitigated locally in every receiver by using built-in testing circuits that measure the receiver gain, and in the transmitter by measuring the transmitted power. However, this approach currently cannot be applied to phase errors. Hence, this thesis assumes that the gain errors are already properly calibrated and only phase errors exist. Among these phase errors in the antenna array, there is one kind of phase error mainly caused by temperature variations between different dies. This kind of phase error between different dies is referred to as inter-die phase error. Besides, a phase error between the antennas within a die also exists, which is referred to as intra-die phase error. The variations of the inter-die phase error between different dies are expected to be larger than the variations of the intra-die phase error between different antenna elements.

Many advanced algorithms, such as Minimum Variance Distortionless Response (MVDR) [1], Estimation of Signal Parameters via Rotational Invariance Technique (ESPRIT) [2], and MUltiple SIgnal Classification (MUSIC) [3], have been developed for DoA estimation, and it is demonstrated that MUSIC outperforms MVDR and ESPRIT in accuracy, stability, and statistical efficiency [4,5]. However, the DoA estimates from these aforementioned algorithms are highly sensitive to the phase errors [6]. These phase errors arise from inherent manufacturing uncertainties, and over time, sensor electronics deviate from their nominal performance mainly due to temperature variations and aging effects, necessitating periodic recalibration, where self-calibration methods are preferred.

Extensive research has been conducted on DoA estimation techniques in the presence of phase uncertainties among antennas [7–12]. In [7–9], the Toeplitz structure of the data covariance matrix was leveraged to exploit redundancies in the uniform geometry, forming an overdetermined system of equations for estimating the calibration parameters. Compared to [7], [8] proposed an additional constraint on phase errors and [9] simplified [7] by using only a few upper triangular entries of the covariance matrix. Besides these redundancy-based self-calibration approaches, [10] proposed an iterative algorithm that solves a nonconvex problem for simultaneously estimating both the DoAs and calibration parameters, and [11] presented a Weighted Alternating Least Squares (WALS) approach for estimating the array parameters, including the DoAs, source and noise powers, and calibration parameters. However, the performance of these two approaches in [10] and [11] is highly dependent on the initial estimate, and it is possible that the algorithm only converges to a local minimum. In [12], a novel convex optimization approach is proposed that decouples the calibration parameters and the DoAs and that allows for the joint estimation of both. It applies the calibration parameters directly to the measurements and assumes that the sources are sparse in the search field (the true DoAs lie on a uniform grid, and the number of grid points is much larger than the number of sources). With additional constraints that describe different antenna and die layouts to incorporate the structural information of the inter-die phase errors, this method shows potential adaptability to the modular approach in imaging radar systems.

In the joint calibration and DoA estimation problem considered in this thesis, there are two types of unknown parameters that need to be estimated: phase errors and DoAs. One type has an impact on the estimation performance of the other. It should come as no surprise that this impact on the estimation performance is dependent on the specific estimation method. To illustrate this cross-impact in a general way, deriving the Cramér-Rao Bound (CRB) is a natural choice, and some works have already used it in the joint calibration and DoA estimation problem for its method-independent nature [11, 13, 14]. Since extensive studies have shown that the CRB has different expressions under different assumptions on the sources (or reflection coefficients) [11, 13–17], choosing appropriate assumptions before any derivation is important. Therefore, this work proposes to first mathematically reveal the assumptions used in the aforementioned works, then choose appropriate assumptions, and, after that, derive the corresponding CRBs.

1.2 Hardware Settings

Figure 1.1 shows the configuration of a radar module made of two transmitter dies and two receiver dies. We assume a total of $M = 16$ transmitting elements, where each transmitter die supports $\frac{M}{2} = 8$ antennas. We further assume $N = 16$ receiver elements, where each receiver die supports $\frac{N}{2} = 8$ antennas. With different routings between dies and antennas, the configuration has an extra degree of freedom to become less sensitive to inter-die phase errors. This thesis focuses on only one routing configuration where the first 8 antennas are connected to the first die and the second 8 antennas to the second die, since in this case, the inter-die phase errors are not averaged out.

In this configuration, the receiving antennas have a uniform spacing $\lambda/2$, and the transmitting antennas have a uniform spacing $N\lambda/2$. The digitized output of all the receivers is processed centrally in a single processor. Phase incoherency, caused by hardware errors, will degrade the performance of DoA estimation. The total phase errors consist of two components: intra-die and inter-die phase errors. Based on the routing configuration used in this thesis, the transmitting or receiving antenna elements from the same die will get the same die-related phase error; the contribution of the inter-die phase errors on the same die is almost perfectly correlated by default. Hence, it is assumed that the inter-die phase errors are the same for the antennas from the same die. The inter-die and intra-die phase errors will have an impact on the DoA estimation performance, for example, a reduction in angular accuracy and dynamic range in the angular domain. Stationary phase errors can be estimated in a calibration setup with known reference targets, and the calibration coefficients can be stored and used as correction values before DoA estimation. However, dynamic effects, such as temperature variations and aging effects, cannot be solved in this way, and signal processing algorithms are required to limit the deteriorating effect on the DoA estimation.

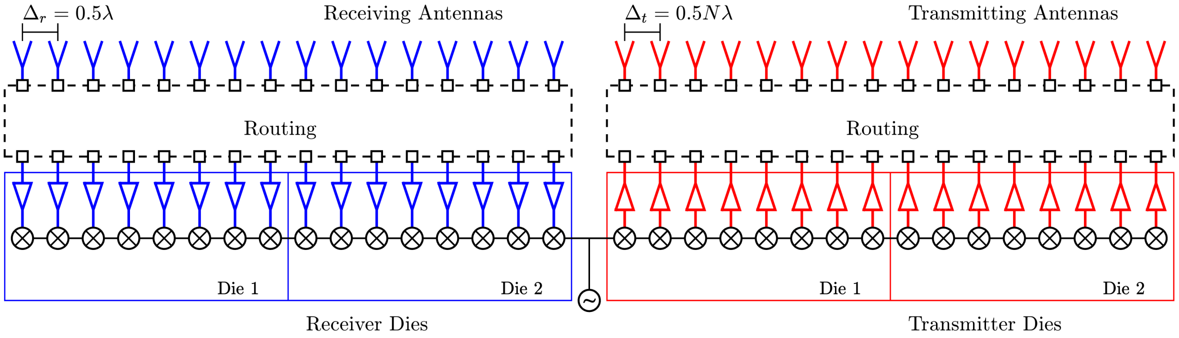

Figure 1.1: An example of the considered hardware configuration. There are $M = 16$ transmitters and $N = 16$ receivers. Each of these is placed on two dies supporting 8 antenna elements per die.

1.3 Signal Model

Consider a one-dimensional colocated MIMO radar system with N receivers, $\Delta_r = \lambda/2$ spaced, and M transmitters, $\Delta_t = N\lambda/2$ spaced, where λ is the source wavelength. Denote the D reflection coefficients from D spatially uncorrelated sources at time t as $\mathbf{s}(t) = [s_1(t), s_2(t), \dots, s_D(t)]^T$. Assuming the targets are far enough from the radar system, the direction of departure is the same as the direction of arrival, which is denoted as θ_d for the dth target. Assuming the narrow-band conditions hold, the matrices containing the steering vectors are defined as:

$$\begin{aligned} \mathbf{A}_r(\boldsymbol{\theta}) &= [\mathbf{a}_r(\theta_1), \mathbf{a}_r(\theta_2), \dots, \mathbf{a}_r(\theta_D)], \\ \mathbf{A}_t(\boldsymbol{\theta}) &= [\mathbf{a}_t(\theta_1), \mathbf{a}_t(\theta_2), \dots, \mathbf{a}_t(\theta_D)], \end{aligned} \tag{1.1}$$

where

$$\begin{aligned}\boldsymbol{\theta} &= [\theta_1, \theta_2, \ldots, \theta_D]^T, \\ [\mathbf{a}_r(\theta_d)]_n &= e^{j2\pi(n-1)\Delta_r \sin\theta_d}, \\ [\mathbf{a}_t(\theta_d)]_m &= e^{j2\pi(m-1)\Delta_t \sin\theta_d}.\end{aligned} \tag{1.2}$$

Assuming orthogonal waveforms are sent by the transmitters and then matched-filtered at the receivers, the resulting NM measurements without phase errors and noise can be expressed as:

$$\begin{aligned}\mathbf{y}(t) &= [\mathbf{A}_r(\boldsymbol{\theta}) \circ \mathbf{A}_t(\boldsymbol{\theta})]\mathbf{s}(t) \\ &= \mathbf{A}(\boldsymbol{\theta})\mathbf{s}(t).\end{aligned} \tag{1.3}$$

However, the phase errors on each antenna will disturb $\mathbf{y}(t)$. For the receiving antennas, denote the intra-die phase error vector as $\hat{\boldsymbol{\gamma}}_r = [e^{j\phi_{r1}}, e^{j\phi_{r2}}, \ldots, e^{j\phi_{rN}}]^T$. Assuming there are K receiver dies, the vector collecting the inter-die phase errors is defined as:

$$\tilde{\boldsymbol{\gamma}}_r = [e^{j\psi_{r1}}, e^{j\psi_{r2}}, \ldots, e^{j\psi_{rK}}]^T. \tag{1.4}$$

There are only K different inter-die phase errors since those errors are related to a die. The total phase error vector for the receiving sensors can then be expressed as:

$$\boldsymbol{\gamma}_r = \hat{\boldsymbol{\gamma}}_r \odot (\tilde{\boldsymbol{\gamma}}_r \otimes \mathbf{1}_{\frac{N}{K}}). \tag{1.5}$$

Similarly, the total phase error vector for the transmitting sensors is:

$$\boldsymbol{\gamma}_t = \hat{\boldsymbol{\gamma}}_t \odot (\tilde{\boldsymbol{\gamma}}_t \otimes \mathbf{1}_{\frac{M}{K}}). \tag{1.6}$$

Incorporating the phase errors and the noise, the received signal vector is then given by:

$$\begin{aligned}\mathbf{x}(t) &= [\boldsymbol{\Gamma}_r\mathbf{A}_r(\boldsymbol{\theta}) \circ \boldsymbol{\Gamma}_t\mathbf{A}_t(\boldsymbol{\theta})]\mathbf{s}(t) + \mathbf{n}(t) \\ &= \boldsymbol{\Gamma}\mathbf{A}(\boldsymbol{\theta})\mathbf{s}(t) + \mathbf{n}(t),\end{aligned} \tag{1.7}$$

where

$$\begin{aligned}\boldsymbol{\Gamma}_r &= \text{diag}(\boldsymbol{\gamma}_r), \\ \boldsymbol{\Gamma}_t &= \text{diag}(\boldsymbol{\gamma}_t), \\ \boldsymbol{\Gamma} &= \text{diag}(\boldsymbol{\gamma}_r \otimes \boldsymbol{\gamma}_t) = \text{diag}(\boldsymbol{\gamma}),\end{aligned} \tag{1.8}$$

and the noise is assumed to be independent and identically distributed following the complex Gaussian distribution, i.e., $\mathbf{n}(t) \sim \mathcal{CN}(\mathbf{0}_{MN}, \sigma_n^2\mathbf{I}_{MN})$. Note here that in the introduced signal model in (1.7), the phase errors $\boldsymbol{\gamma}$ and the DoAs $\boldsymbol{\theta}$ can also change over time, but much more slowly than the rest.

1.4 Problem Statement

DoA estimation is one of the main tasks of automotive imaging radar systems. In a dynamic environment, the DoA estimation algorithm is supposed to perform in real time to adapt to moving targets. Moreover, periodic recalibration is required since the dynamic phase errors have an impact on the performance of DoA estimation in real time.

Considering the scenario of starting an automobile, the environment around it is completely unknown: an unknown number of targets and DoAs. Besides, the phase errors are completely different from those at the last time starting. Jointly estimating the parameters of interest from scratch at every time step can be difficult since a large amount of computing time required in each radar cycle can cause the system to be unable to accurately estimate DoAs in real time. Hence, this work proposes to divide the entire process into two stages and apply a two-step approach to tackle the joint calibration and DoA estimation problem.

1.4.1 Stage 1: Static Stage

The duration of this stage is assumed to be short enough, e.g., 10 radar cycles, so that the time-varying effects, i.e., the temperature variations and the aging effects, can be ignored, and the phase errors are static. Besides, it is assumed that the automobile is not moving and that the targets are static. These are fair assumptions, since, in real life, this stage takes only a few seconds, the time-varying effects, i.e., the temperature variations and the aging effects, can be considered minimal. Besides, what usually happens is that an automobile is parked in an environment surrounded by static objects, whereas parking in places with moving objects is not a good idea. Based on these assumptions, the main goal in this stage is to obtain a reasonable initial estimate of phase errors with multiple measurements and, besides, to perform DoA estimation.

Under the assumptions in this stage, the signal model in (1.7) can be expressed with multiple measurements. For notational convenience, denote $\mathbf{A} = \mathbf{A}(\boldsymbol{\theta})$. With the static phase errors during one observation window where T measurements are collected from T radar cycles, the signal model (1.7) becomes:

$$\mathbf{X} = \boldsymbol{\Gamma}\mathbf{A}\mathbf{S} + \mathbf{N}, \tag{1.9}$$

where

$$\begin{aligned} \mathbf{X} &= [\mathbf{x}(0), \mathbf{x}(1), \ldots, \mathbf{x}(T-1)], \\ \mathbf{S} &= [\mathbf{s}(0), \mathbf{s}(1), \ldots, \mathbf{s}(T-1)], \\ \mathbf{N} &= [\mathbf{n}(0), \mathbf{n}(1), \ldots, \mathbf{n}(T-1)]. \end{aligned} \tag{1.10}$$

1.4.2 Stage 2: Varying Stage

In this stage, the time-varying effects, i.e., temperature variations and aging effects, begin to influence the antennas. Hence, the phase errors are slowly varying over time. The goal in this stage is to estimate both the phase errors and the DoAs utilizing the initial estimate of the phase errors from stage 1 at each radar cycle, and hence, a fast algorithm that can adapt to changes in the phase errors is required. Because the phase errors can vary in each radar cycle, the corresponding signal model in this stage is given by (1.7).

1.5 Disturbed Beampatterns in the Two Estimation Stages

To better illustrate the necessity of the calibration task under the aforementioned hardware setting in the two stages, beampatterns with phase errors in the two stages are plotted and shortly analyzed. Before the beampattern simulations, the model to simulate the slowly varying phase errors is first introduced.

1.5.1 Slowly Varying Phase Error Model

Consider the phase of the total complex phase error on the mth antenna of the kth die in the static environment, denoted as $\varphi_{mk0} = \phi_{rm} + \psi_{rk}$. Here, ϕ and ψ represent the phases of the complex intra-die and inter-die phase errors, respectively. Since there is currently no real data illustrating the characteristics of the varying phases of the complex errors, it is assumed to be time-correlated, and this time-correlation between two realizations of the phase errors attenuates over time. Hence, the phase at time index t can be expressed as:

$$\varphi_{mk}(t) = \varphi_{mk0} + \Delta\varphi_k(t), \tag{1.11}$$

where $\Delta\varphi_k(t)$ is the slowly varying phase component of the total complex phase errors. Since this varying component is mainly caused by the temperature variations, it is assumed to be the same within the same die. Now the goal is to model $\Delta\varphi_k(t)$. It is assumed to be the output of the convolution between a white Gaussian process $w_k(t)$ with power spectral density δ^2 and an exponential attenuation function $h(t)$:

$$\Delta\varphi_k(t) = w_k(t) \circledast h(t), \tag{1.12}$$

where

$$h(t) = \sqrt{2R_0\frac{\alpha}{\tau}e^{-\frac{\alpha}{\tau}t}u(t)}, \tag{1.13}$$

with $u(t)$ the unit step function, and α, τ, and $R_0 > 0$. It can be shown that the autocorrelation function of $\Delta\varphi_k(t)$ is then given by:

$$R_{\Delta\phi_k}(t) = \delta^2 R_0 e^{-\alpha\frac{|t|}{\tau}}. \tag{1.14}$$

An example of the normalized autocorrelation function and the slowly varying phase components is shown in Figure 1.2, with $\alpha/\tau = 0.2$ and $\delta = 0.05$.

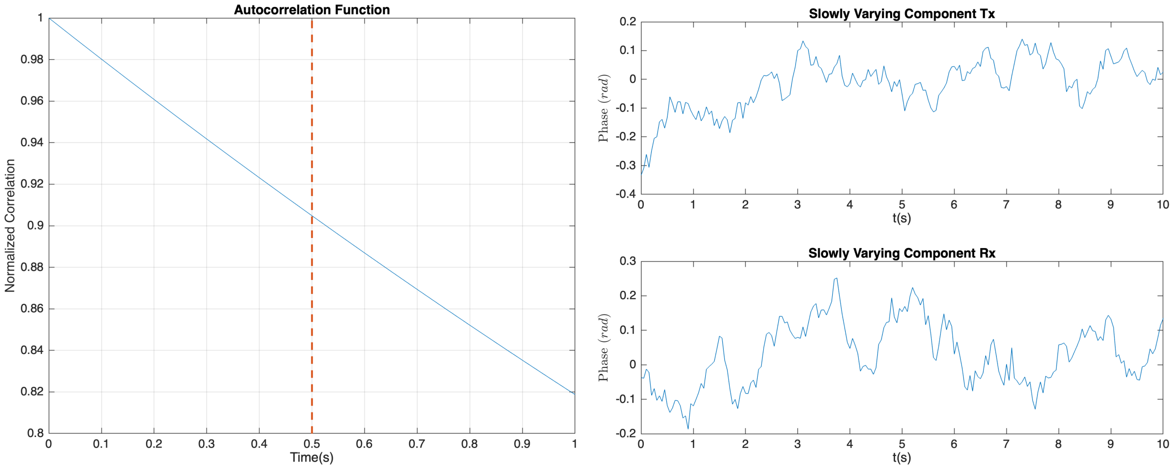

(a) Normalized autocorrelation function, with $\alpha/\tau = 0.2$ and $\delta = 0.05$.

(b) One realization of the slowly varying phase components, with $\alpha/\tau = 0.2$ and $\delta = 0.05$.

Figure 1.2: An example of the autocorrelation function and slowly varying phase components, $\alpha/\tau = 0.2$ and $\delta = 0.05$. The red dashed line represents the time index corresponding to 10 radar cycles.

1.5.2 Beampatterns

Figure 1.4 shows the simulation of the beampatterns from the uncalibrated array and that from the array without phase errors. In Figure 1.4(b), 40 realizations of static phase errors are applied, where the phases of the complex inter-die and intra-die errors are drawn from a white Gaussian process with standard deviation $\sigma_{\text{inter}} = 10°$ and $\sigma_{\text{intra}} = 0.7°$, respectively. In Figure 1.4(c), 1000 realizations of slowly varying phase components are drawn from the slowly varying phase error model with $\alpha/\tau = 0.2$ and $\delta = 0.05$.

Zooming in on Figure 1.4(a), the mainlobe and the two nearest sidelobes can be observed more clearly, shown in Figure 1.3. The $-3dB$ width of the mainlobe is calculated to evaluate the average Mainlobe Width (MW). Besides, the average Sidelobe Levels (SLs) in dB are also calculated, where the sidelobe is the one nearest to the mainlobe in Figure 1.3. Moreover, compared to the beampattern without phase errors shown in Figure 1.4(a), it can be observed that there are many high-level peaking sidelobes on both sides of the main lobe. The average values of the four highest Peaking Sidelobe Levels (PSLs) on the positive-value-angle side are also calculated.

The aforementioned results are shown in Table 1.1. It can be seen that both types of phase errors have no effect on the MW, and the effect on the SLs is minimal, compared to that on the PSLs. These peaking sidelobes can lead to false target detections in the angular domain. Even if a relatively higher threshold is applied to discard the false detections, the dynamic range for effective detection is reduced. Hence, suppressing these peaking sidelobes generated by the phase errors is necessary.

Phase Error Type	MW (°)	SL (dB)	PSL1 (dB)	PSL2 (dB)	PSL3 (dB)	PSL4 (dB)
No	0.67	-13.41	-54.13	-45.05	-49.24	-55.93
Static	0.67	-13.35	-22.51	-31.53	-35.23	-36.51
Slowly Varying	0.67	-13.06	-19.54	-29.05	-32.66	-34.45

Table 1.1: Average values of mainlobe width, sidelobe levels, and peaking sidelobe levels from the array without and with phase errors.

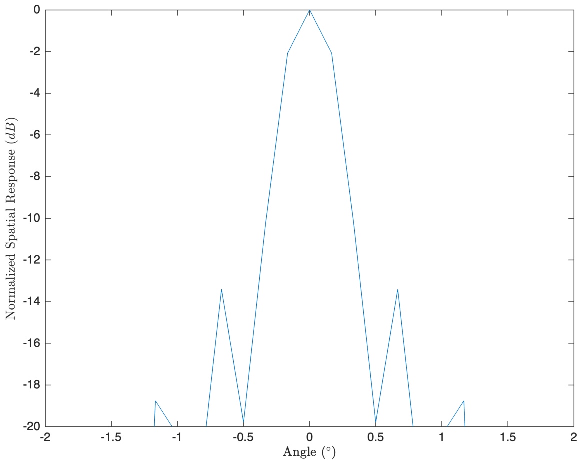

Figure 1.3: Zoomed-in beampattern of the array without phase errors.

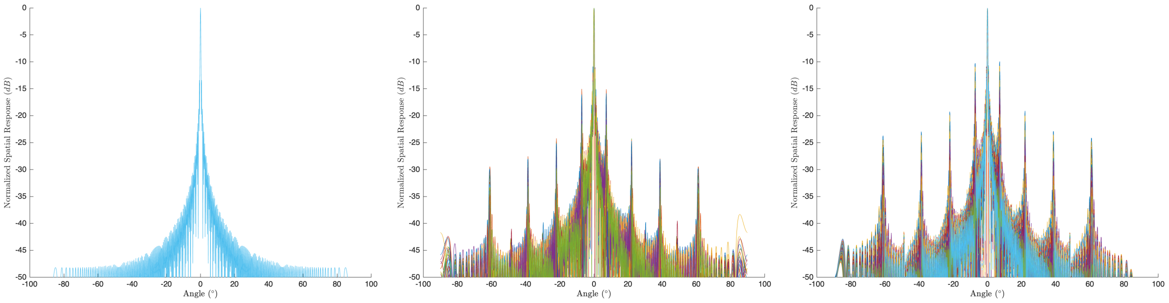

(a) Beampattern aiming at broadside without phase errors.

(b) Beampatterns on top of each other, aiming at broadside with 40 static phase error realizations.

(c) Beampatterns on top of each other, aiming at broadside with 1000 slowly varying phase error realizations.

Figure 1.4: Beampatterns aiming at broadside of the uncalibrated array.

1.6 Thesis Outline

The remainder of this thesis is as follows:

- **Chapter 2:** The two-step approach for solving the joint calibration and DoA estimation problem is derived. In the first step, a convex optimization problem incorporating the die structure-based constraint on the inter-die phase errors is formulated. In the second step, an alternating approach with a subspace tracking technique is elaborated.

- **Chapter 3:** Experimental results of the proposed two-step approach are discussed, simulations of the beampatterns from the calibrated array are performed, and a dynamic range test is conducted to illustrate the effectiveness of the proposed approach.
- **Chapter 4:** The assumptions on the reflection coefficients are motivated after revealing the relation between different CRB expressions under different assumptions. Next, the CRB is derived under the selected assumptions.
- **Chapter 5:** The cross-impact between the phase errors and the DoAs is analysed based on the derived CRBs.
- **Chapter 6:** Conclusions of this thesis and suggestions for possible future work.

2

The Two-Step Approach

This chapter elaborates on the two-step approach. The two steps aim to jointly calibrate antennas and estimate DoAs in the corresponding stages. In Section 2.1, the convex optimization approach for stage 1 is derived with a simplified phase error structure that decreases the number of unknown parameters. Section 2.2 derives the alternating update approach for stage 2, which alternately estimates the DoAs and the phase errors in each iteration.

2.1 Step 1: Die Structure-Based Convex Optimization Approach

At this stage, the DoAs and the phase errors are both static. The only information available is the sparsity assumption on the targets and the die-related structure of the phase errors. The convex optimization approach aims to estimate the number of targets, the DoAs of the targets, and, most importantly, the initial phase errors. In the derivation, since there are more unknowns than equations, the system of equations cannot be solved. Hence, this approach proposes to use a Kronecker-product structure to model the phase errors by considering the intra-die phase errors as noise and only considering the inter-die phase errors as the parameters of interest. By doing so, the system of equations can be solved.

Assuming that the true DoAs are drawn from a uniform grid of $P \gg D$ points, i.e., $\theta_d \in \{-\frac{\pi}{2}, -\frac{\pi}{2}+\frac{\pi}{P}, \dots, -\frac{\pi}{2}+\frac{(P-1)\pi}{P}\}$ for $d = 1, 2, \dots, D$, and collecting the angles of the points on the grid in a vector, i.e., $\tilde{\boldsymbol{\theta}} = [-\frac{\pi}{2}, -\frac{\pi}{2}+\frac{\pi}{P}, \dots, -\frac{\pi}{2}+\frac{(P-1)\pi}{P}]^T$, the signal model in (1.9) can be approximated as:

$$\mathbf{G}\mathbf{X} = \tilde{\mathbf{A}}\tilde{\mathbf{S}} + \mathbf{N}, \tag{2.1}$$

where

$$\begin{aligned} \tilde{\theta}_p &= \frac{(p-1)\pi}{P}, \\ \mathbf{G} &= \operatorname{diag}(\mathbf{g}) = \boldsymbol{\Gamma}^{-1}, \\ \tilde{\mathbf{A}} &= [\mathbf{a}(\tilde{\theta}_1), \mathbf{a}(\tilde{\theta}_2), \dots, \mathbf{a}(\tilde{\theta}_P)], \\ \tilde{\mathbf{S}} &= [\tilde{\mathbf{s}}(0), \tilde{\mathbf{s}}(1), \dots, \tilde{\mathbf{s}}(T-1)] \\ &= [\tilde{\mathbf{s}}_1, \tilde{\mathbf{s}}_2, \dots, \tilde{\mathbf{s}}_P]^T. \end{aligned} \tag{2.2}$$

Note here that $\tilde{\mathbf{S}}$ is a $P \times T$ matrix with rows corresponding to the actual DoAs being the reflection coefficients and other rows being all zeros. Furthermore, we do not change the notation for the matrix $\mathbf{N}$ since its distribution did not change. The purpose of applying the inverse of the diagonal phase error matrix $\mathbf{G}$ is to decouple the calibration parameters from the DoAs.

By rewriting (2.1) as:

$$\underbrace{\left[\begin{array}{c|ccc} \mathrm{diag}(\mathbf{x}(0)) & -\tilde{\mathbf{A}} & & \\ \vdots & & \ddots & \\ \mathrm{diag}(\mathbf{x}(T-1)) & & & -\tilde{\mathbf{A}} \end{array}\right]}_{\mathbf{H}} \underbrace{\left[\begin{array}{c} \mathbf{g} \\ \hline \tilde{\mathbf{s}} \end{array}\right]}_{\boldsymbol{\rho}} = \underbrace{\begin{bmatrix} \mathbf{n}(0) \\ \vdots \\ \mathbf{n}(T-1) \end{bmatrix}}_{\tilde{\mathbf{n}}}, \tag{2.3}$$

where $\tilde{\mathbf{s}} = \mathrm{vec}(\tilde{\mathbf{S}})$, a linear system of equations can be solved. More specifically, the system of equations in (2.3) can be solved with a reference channel (a known element of $\boldsymbol{\gamma}$ or $\mathbf{g}$) and a known reference signal [12], but in the situation considered in this thesis, there is no known reference signal. However, since the variations of the phase errors between dies are expected to be much larger than the variations between antennas, viewing the intra-die phase errors as noise is a good choice to decrease the number of unknown variables. Besides, since the inter-die phase errors have die-related structural information, an additional constraint on the inter-die phase errors can be incorporated.

First, viewing the intra-die phase errors as random complex noise and considering only the inter-die phase errors as parameters of interest, the total phase errors can be expressed as:

$$\begin{aligned} \boldsymbol{\gamma} &= [\hat{\boldsymbol{\gamma}}_r \odot (\tilde{\boldsymbol{\gamma}}_r \otimes \mathbf{1}_{\frac{N}{K}})] \otimes [\hat{\boldsymbol{\gamma}}_t \odot (\tilde{\boldsymbol{\gamma}}_t \otimes \mathbf{1}_{\frac{M}{K}})] \\ &= [(\tilde{\boldsymbol{\gamma}}_r \otimes \mathbf{1}_{\frac{N}{K}}) \otimes (\tilde{\boldsymbol{\gamma}}_t \otimes \mathbf{1}_{\frac{M}{K}})] \odot (\hat{\boldsymbol{\gamma}}_r \otimes \hat{\boldsymbol{\gamma}}_t) \\ &= [(\tilde{\boldsymbol{\gamma}}_r \otimes \mathbf{1}_{\frac{N}{K}}) \otimes (\tilde{\boldsymbol{\gamma}}_t \otimes \mathbf{1}_{\frac{M}{K}})] \odot \mathbf{n}_\gamma, \end{aligned} \tag{2.4}$$

where $\mathbf{n}_\gamma = \hat{\boldsymbol{\gamma}}_r \otimes \hat{\boldsymbol{\gamma}}_t$ yields the total intra-die phase error vector viewed as noise.

Following that, since there are K receiver dies and K transmitter dies, the number of different inter-die phase errors is $2K$ in total. With the Kronecker product, the number of different product combinations of the inter-die phase errors in $\boldsymbol{\gamma}$ is K^2. By collecting these combinations into a vector $\boldsymbol{\gamma}_{rt}$, the phase error vector can be further expressed as:

$$\boldsymbol{\gamma} = \begin{bmatrix} \mathbf{1}_{\frac{N}{K}} \otimes \left(\begin{bmatrix} [\boldsymbol{\gamma}_{rt}]_1 \\ \vdots \\ [\boldsymbol{\gamma}_{rt}]_K \end{bmatrix} \otimes \mathbf{1}_{\frac{M}{K}} \right) \\ \vdots \\ \mathbf{1}_{\frac{N}{K}} \otimes \left(\begin{bmatrix} [\boldsymbol{\gamma}_{rt}]_{K^2-K+1} \\ \vdots \\ [\boldsymbol{\gamma}_{rt}]_{K^2} \end{bmatrix} \otimes \mathbf{1}_{\frac{M}{K}} \right) \end{bmatrix} \odot \mathbf{n}_\gamma. \tag{2.5}$$

Likewise, $\mathbf{g}$ can be written in the same form. By incorporating a reference phase error to avoid the same phase shift for all channels, a convex optimization problem can be formulated to jointly estimate the calibration parameters and the DoAs:

$$\begin{aligned}
\min_{\mathbf{g}_{rt},\tilde{\mathbf{s}}} \quad & \|\mathbf{H}\boldsymbol{\rho}\|_2^2 + \lambda f(\tilde{\mathbf{s}}) \\
s.t. \quad & f(\tilde{\mathbf{s}}) = \|\tilde{\mathbf{s}}^{(2)}\|_1 \\
& \tilde{\mathbf{s}}^{(2)} = \big[\|\tilde{\mathbf{s}}_1\|_2, \|\tilde{\mathbf{s}}_2\|_2, \ldots, \|\tilde{\mathbf{s}}_P\|_2\big]^T \\
& [\hat{\mathbf{g}}]_1 = c, \\
& |[\mathbf{g}_{rt}]_i| \leq 1, \quad \forall i = 1, 2, \ldots, K^2 \\
& \hat{\mathbf{g}} = \begin{bmatrix} \mathbf{1}_{\frac{N}{K}} \otimes \left(\begin{bmatrix} [\mathbf{g}_{rt}]_1 \\ \vdots \\ [\mathbf{g}_{rt}]_K \end{bmatrix} \otimes \mathbf{1}_{\frac{M}{K}} \right) \\ \vdots \\ \mathbf{1}_{\frac{N}{K}} \otimes \left(\begin{bmatrix} [\mathbf{g}_{rt}]_{K^2-K+1} \\ \vdots \\ [\mathbf{g}_{rt}]_{K^2} \end{bmatrix} \otimes \mathbf{1}_{\frac{M}{K}} \right) \end{bmatrix},
\end{aligned} \tag{2.6}$$

where $\hat{\mathbf{g}}$ is the estimate of $\mathbf{g}$, and c is a constant with the value equal to $[\boldsymbol{\gamma}]_1^{-1}$. λ is the regularization parameter that balances the trade-off between the goodness of the fit of the solution to the given data and the sparsity prior on $\tilde{\mathbf{s}}$. The inequality $[\mathbf{g}_{rt}]_i \leq 1$ is to constrain the amplitudes of the calibration parameters.

2.2 Step 2: PAST-Based Alternating Update Approach

Up to this stage, a reasonable initial estimate of the phase errors is available from stage 1. The phase errors begin varying, and the goal of this alternating update approach is to alternately estimate the slowly varying phase errors and the DoAs in each radar cycle.

At the beginning of this procedure, the initial estimates of the phase error matrix $\hat{\boldsymbol{\Gamma}}^{(0)}$, number of sources $\hat{D}^{(0)}$ and DoAs $\hat{\boldsymbol{\theta}}^{(0)} = [\hat{\theta}_1^{(0)}, \hat{\theta}_2^{(0)}, \ldots, \hat{\theta}_D^{(0)}]^T$ are available from stage 1, and there are at least T measurements collected from stage 1. Hence, the initial covariance matrix of the measurements $\hat{\mathbf{R}}_x^{(0)}$ can be obtained. The idea of this procedure is to iteratively update those estimates from the previous results with the newly collected measurement.

At the tth iteration, we first estimate the measurement covariance matrix $\hat{\mathbf{R}}_x^{(t)} = \beta_f \hat{\mathbf{R}}_x^{(t-1)} + \mathbf{x}(t)\mathbf{x}^H(t)$, where $\mathbf{x}(t)$ is the new measurement collected at the current iteration, and β_f is a forgetting factor $0 < \beta_f \leq 1$ to down-weigh the measurements in the distant past in order to afford the tracking capability when the system operates in a nonstationary environment. Setting $\beta_f = 1$ represents the growing sliding window case. After that, we perform an EigenValue Decomposition (EVD) of $\hat{\mathbf{R}}_x^{(t)}$ to find the eigenvectors spanning the noise subspace $\hat{\mathbf{U}}_n^{(t)}$ of dimension $NM - \hat{D}^{(t-1)}$.

Then, we are ready to estimate the DoAs. We set a threshold β and search for all peaks higher than β in the MUSIC pseudo-spectrum:

$$P^{(t)}(\theta) = \|\hat{\mathbf{U}}_n^{(t)H}\hat{\mathbf{\Gamma}}^{(t-1)}\mathbf{a}(\theta)\|^{-2}. \tag{2.7}$$

Those peaks that are higher than β are associated with the new DoAs $\hat{\boldsymbol{\theta}}^{(t)}$, and their number is the estimated number of targets at time step t, $\hat{D}^{(t)}$.

Following that, now fix the DoAs and minimize the loss function $L^{(t)}$ with respect to the phase errors:

$$\begin{aligned} \min_{\boldsymbol{\gamma}} \quad L^{(t)} &= \sum_{d=1}^{\hat{D}^{(t)}} \|\hat{\mathbf{U}}_n^{(t)H}\mathbf{\Gamma}\mathbf{a}(\hat{\theta}_d^{(t)})\|^2 \\ &= \|[\sum_{d=1}^{\hat{D}^{(t)}} \hat{\mathbf{U}}_n^{(t)H}\mathrm{diag}(\mathbf{a}(\hat{\theta}_d^{(t)}))]\boldsymbol{\gamma}\|^2, \\ s.t. \quad \mathbf{w}^T\boldsymbol{\gamma} &= 1, \end{aligned} \tag{2.8}$$

where $\mathbf{w} = [1, 0, 0, \dots, 0]^T$. The solution is well known and given by:

$$\tilde{\boldsymbol{\gamma}}^{(t)} = \frac{(\mathbf{Z}^{(t)})^{-1}\mathbf{w}}{\mathbf{w}^T(\mathbf{Z}^{(t)})^{-1}\mathbf{w}}, \tag{2.9}$$

where $\mathbf{Z}^{(t)}$ is the matrix:

$$\mathbf{Z}^{(t)} = \sum_{d=1}^{\hat{D}^{(t)}} \mathrm{diag}(\mathbf{a}(\hat{\theta}_d^{(t)}))^H\hat{\mathbf{U}}_n^{(t)}\hat{\mathbf{U}}_n^{(t)H}\mathrm{diag}(\mathbf{a}(\hat{\theta}_d^{(t)})). \tag{2.10}$$

Since it is assumed that there are no gain errors, $\tilde{\boldsymbol{\gamma}}^{(t)}$ can be further projected to satisfy the norm constraint according to:

$$[\hat{\boldsymbol{\gamma}}^{(t)}]_i = \mathcal{P}([\tilde{\boldsymbol{\gamma}}^{(t)}]_i) = \frac{[\tilde{\boldsymbol{\gamma}}^{(t)}]_i}{|[\tilde{\boldsymbol{\gamma}}^{(t)}]_i|}, \quad \text{for } i = 1, 2, \dots, NM. \tag{2.11}$$

Here, to also estimate the intra-die phase errors, the Kronecker product structure is not incorporated. Up to this point, an algorithm based on the EVD has been developed to update the DoAs and phase errors. However, the EVD can be computationally expensive, and therefore, a subspace tracking algorithm called PAST [18,19] is applied to replace the EVD.

Instead of updating the covariance matrix of the measurements and calculating $\hat{\mathbf{U}}_n^{(t)}$ by the EVD, PAST directly updates the signal subspace $\hat{\mathbf{U}}_s^{(t)}$ using the new measurement by solving the following loss function with respect to $\hat{\mathbf{U}}_s^{(t)}$:

$$L_p^{(t)} = \sum_{i=1}^{t} \beta_f^{t-i}||\mathbf{x}(i) - \hat{\mathbf{U}}_s^{(t)}\mathbf{p}(i)||^2, \tag{2.12}$$

where $\mathbf{p}(i) = \hat{\mathbf{U}}_s^{(i-1)H}\mathbf{x}(i)$, which is the approximation of the projection of $\mathbf{x}(i)$ onto the columns of $\hat{\mathbf{U}}_s^{(t)}$. One only needs to change two aspects in the aforementioned alternating algorithm to use the PAST. First, calculate $\hat{\mathbf{U}}_s^{(0)}$ using the EVD and $\mathbf{P}^{(0)} = (\hat{\mathbf{U}}_s^{(0)H}\hat{\mathbf{R}}_x^{(0)}\hat{\mathbf{U}}_s^{(0)})^{-1}$. Then, in each iteration, use the new measurement directly to update $\mathbf{P}^{(t)}$ and $\hat{\mathbf{U}}_s^{(t)}$ according to:

$$\begin{aligned}
\mathbf{p}(t) &= \hat{\mathbf{U}}_s^{(t-1)H}\mathbf{x}(t), \\
\mathbf{h}(t) &= \mathbf{P}^{(t-1)}\mathbf{p}(t), \\
\mathbf{q}(t) &= \frac{\mathbf{h}(t)}{\beta_f + \mathbf{p}^H(t)\mathbf{h}(t)}, \\
\mathbf{P}^{(t)} &= \frac{1}{\beta_f}[\mathbf{P}^{(t-1)} - \mathbf{q}(t)\mathbf{p}^H(t)], \\
\mathbf{e}(t) &= \mathbf{x}(t) - \hat{\mathbf{U}}_s^{(t-1)}\mathbf{p}(t), \\
\hat{\mathbf{U}}_s^{(t)} &= \hat{\mathbf{U}}_s^{(t-1)} + \mathbf{e}(t)\mathbf{q}^H(t),
\end{aligned} \tag{2.13}$$

where $\mathbf{h}(t)$, $\mathbf{q}(t)$, and $\mathbf{e}(t)$ are the intermediate variables to avoid inverting matrices in the calculation of $\mathbf{P}^{(t)}$ [19].

After obtaining $\hat{\mathbf{U}}_s^{(t)}$, the following steps are just the same as described in (2.7) – (2.11). Note here that in the derivation in (2.7) – (2.11), instead of $\hat{\mathbf{U}}_n^{(t)}$, what is needed is $\hat{\mathbf{U}}_n^{(t)}\hat{\mathbf{U}}_n^{(t)H}$, and with the obtained $\hat{\mathbf{U}}_s^{(t)}$ from the PAST, this can be computed by observing that $\hat{\mathbf{U}}_s^{(t)}\hat{\mathbf{U}}_s^{(t)H} + \hat{\mathbf{U}}_n^{(t)}\hat{\mathbf{U}}_n^{(t)H} = \mathbf{I}$. By utilizing PAST, the computational complexity is reduced to $\mathcal{O}(D^2) + 3MND$ at each iteration, which is much lower compared to $\mathcal{O}(M^3N^3)$ for the EVD.

2.3 Conclusions

In this chapter, the proposed two-step approach is presented. For stage 1, the die structure-based convex optimization approach is derived. In this approach, multiple snapshots are collected to jointly calibrate the antennas and estimate the DoAs. The intra-die phase errors are viewed as noise since the variations of these errors are much smaller than those of the inter-die phase errors, and a constraint on the inter-die phase error structure is developed to decrease the number of unknown parameters, which makes the convex optimization problem possible to solve. The PAST-based alternating update approach is developed for stage 2, which utilizes each newly collected measurement to update the estimates of the phase errors and the DoAs, based on the initial estimates from stage 1. In this approach, the measurement subspace calculation is relying on the PAST algorithm instead of the EVD. By doing so, the computational complexity required for the subspace calculation is dramatically reduced.

Simulation Results

3

To validate the effectiveness of the proposed approach, simulation experiments are conducted in this chapter. Section 3.1 analyzes the Root Mean Square Errors (RMSEs) of the estimation results from the die structure-based convex optimization approach for stage 1, i.e., the row norms and phase errors. Section 3.2 discusses the performance of the PAST-based alternating update approach by evaluating the RMSEs of the estimated phase errors and DoAs. In Section 3.3, the average $-3dB$ mainlobe width, sidelobe levels, and the peaking sidelobe levels of the beampatterns from the calibrated array are analyzed to show the effectiveness of the proposed approach. Section 3.4 tests the performance of the proposed approach in estimating two targets that are close to each other and have a dramatic difference between their SNR levels in both stages.

3.1 Step 1: Estimation Results

In this section, the die structure-based convex optimization approach is tested on different values of σ_{inter} and σ_{intra}. The RMSE is applied to the estimates of the row norms and the phase errors, and the MUSIC spectra are shown as illustrations of the estimation. Two realizations of the DoAs are selected: (i) $[-85.5°, -80.5°, -75.5°]^T$ and (ii) $[-5°, 0°, 5°]^T$. (i) is chosen since the targets around the boundaries of the Field of View (FoV) are usually difficult to estimate, and thus can illustrate the performance in a relatively worse case. (ii) contains the targets from the broadside of the FoV, which is the usual case of interest. The following parameters are fixed: $M = N = 16$, $K = 2$, $T = 10$, $D = 3$, and SNR $= 10dB$. The target strengths are the same.

Figure 3.1 shows the results of the die structure-based convex optimization approach, where $\sigma_{\text{intra}} = 0.7°$ and $\sigma_{\text{inter}} = 10°$. In Figure 3.1(a) and Figure 3.1(c), a threshold is applied to select only those peaks higher than the threshold to identify the correct number of targets. It can be seen that for the targets around the broadside, the selected peaks represent the DoAs exactly, and for those close to the FoV boundary, only the one closest to the FoV boundary is not exact. This inaccuracy can be explained by the bias caused by the regularizer. In both cases, the number of targets can be exactly identified. Then, the MUSIC algorithm is used to identify the DoAs after the estimated $\boldsymbol{\gamma}$ (or $\mathbf{g}$) is applied to the measurements, shown in Figure 3.1(b) and Figure 3.1(d). It can be seen that the DoAs can be identified exactly.

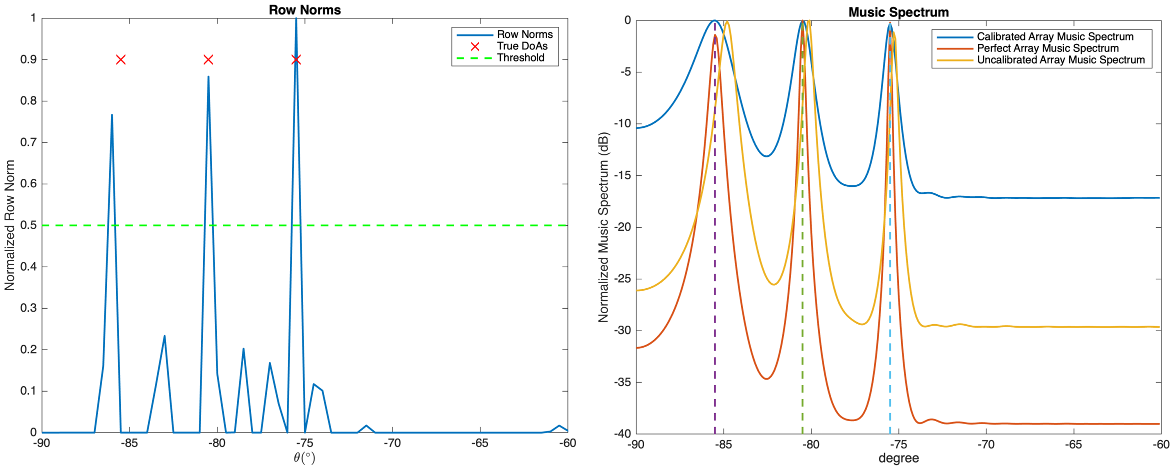

(a) Estimated row norms. DoAs are −85.5°, −80.5° and −75.5°.

(b) Music spectrum, DoAs are −85.5°, −80.5° and −75.5°.

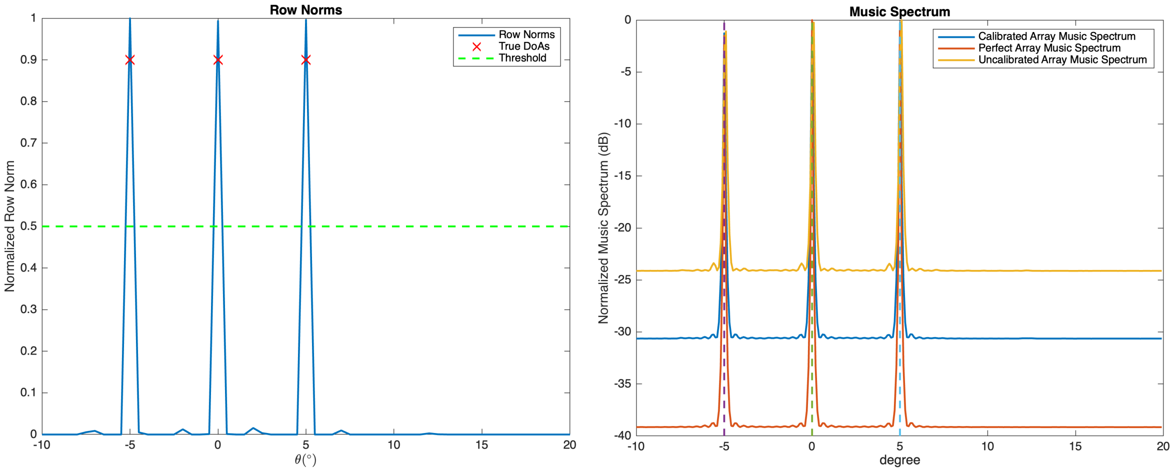

(c) Estimated row norms, DoAs are −5°, 0° and 5°.

(d) Music spectrum, DoAs are −5°, 0° and 5°.

Figure 3.1: Results of the die structure-based convex optimization, $\sigma_{\text{inter}} = 10^\circ$, $\sigma_{\text{intra}} = 0.7^\circ$.

To show the performance of the proposed approach under the influence of different intra-die and inter-die phase error variations, three additional combinations of $\{\sigma_{intra}, \sigma_{inter}\}$, i.e., $\{0.7^\circ, 20^\circ\}$, $\{5^\circ, 20^\circ\}$ and $\{10^\circ, 20^\circ\}$, are applied to the proposed approach. The RMSEs of the estimation results and the values of the corresponding parameters are shown in Table 3.1 and Table 3.2, where the DoAs are $\{-85.5^\circ$, -80.5°, $-75.5^\circ\}$ and $\{-5^\circ$, 0°, $5^\circ\}$, respectively. Interestingly, according to the RMSEs when $\sigma_{intra} = 0.7^\circ$ in Table 3.1 and Table 3.2, increasing only σ_{inter} does not influence the RMSEs too much, despite the RMSE of $\tilde{\mathbf{s}}^{(2)}$ when the targets are close to the FoV boundary, and according to Figure 3.2(a), Figure 3.3(a), Figure 3.2(d), and Figure 3.3(d), the estimated row norms and the MUSIC spectrum look similar to those with the corresponding DoAs in Figure 3.1. It seems that the inter-die standard deviation does not have an obvious influence on the performance of the proposed approach. This is consistent with the focus in this stage: estimating only the inter-die phase errors and providing reasonable initial estimates. These results demonstrate the effectiveness of the proposed approach in this initial stage, with a small intra-die standard deviation.

Since the proposed approach focuses only on the inter-die phase errors, the performance can be influenced by the intra-die phase errors. According to Table 3.1 and Table 3.2, when $\sigma_{inter} = 20°$, the RMSEs for both $\mathbf{g}$ and $\tilde{\mathbf{s}}^{(2)}$ become higher with the increase of σ_{intra}, and in the plots of the row norms in Figure 3.2 and Figure 3.3, higher peaks around the true DoAs can be observed. Undoubtedly, the estimated row norms and the phase errors are not as good as before. However, according to the MUSIC spectrum in Table 3.1 and Table 3.2, the true DoAs can still be identified. These results illustrate the effectiveness of focusing on only the inter-die phase errors and the robustness of the proposed approach to disturbances of the intra-die phase errors.

σ_{intra}	σ_{inter}	RMSE of $\mathbf{g}$	λ	RMSE of $\tilde{\mathbf{s}}^{(2)}$
0.7	10	0.446	30	0.072
0.7	20	0.447	30	0.067
5	20	0.554	50	0.079
10	20	0.703	75	0.106

Table 3.1: Parameters and RMSEs of the joint calibration and DoA estimation. DoAs are $-85.5°$, $-80.5°$ and $-75.5°$.

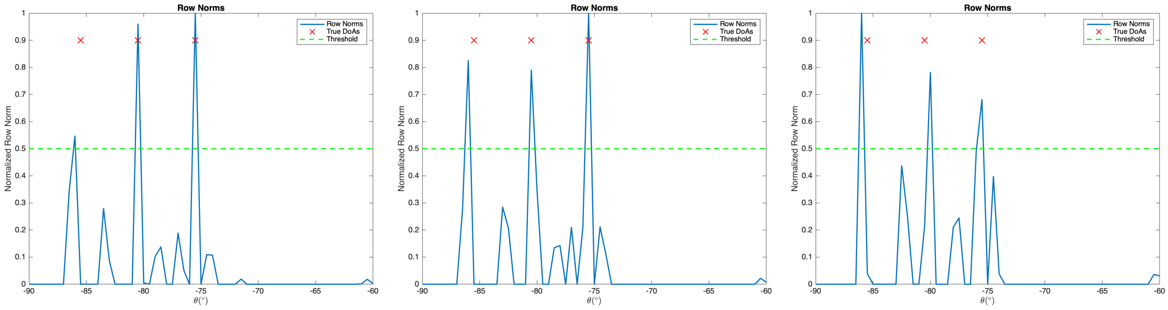

(a) Estimated row norms, $\sigma_{\text{inter}} = 20°$, $\sigma_{\text{intra}} = 0.7°$.

(b) Estimated row norms, $\sigma_{\text{inter}} = 20°$, $\sigma_{\text{intra}} = 5°$.

(c) Estimated row norms, $\sigma_{\text{inter}} = 20°$, $\sigma_{\text{intra}} = 10°$.

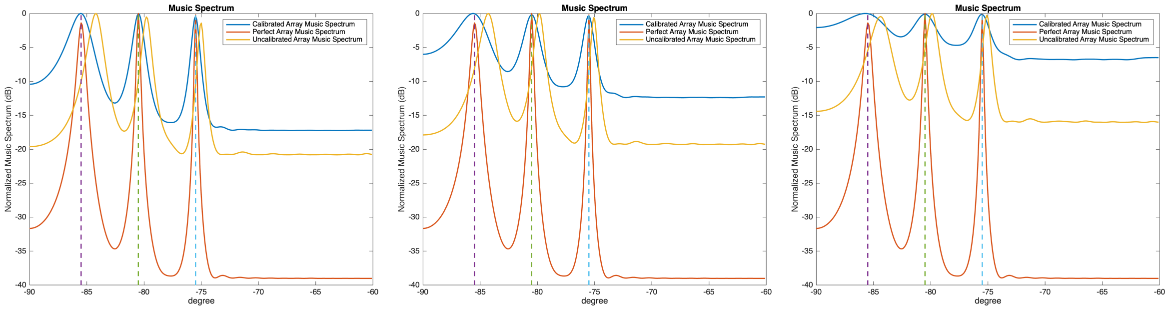

(d) MUSIC spectrum, $\sigma_{\text{inter}} = 20°$, $\sigma_{\text{intra}} = 0.7°$.

(e) MUSIC spectrum, $\sigma_{\text{inter}} = 20°$, $\sigma_{\text{intra}} = 5°$.

(f) MUSIC spectrum, $\sigma_{\text{inter}} = 20°$, $\sigma_{\text{intra}} = 10°$.

Figure 3.2: Estimated row norms and the MUSIC spectrum, DoAs are $-85.5°$, $-80.5°$ and $-75.5°$.

σ_{intra}	σ_{inter}	RMSE of $\mathbf{g}$	λ	RMSE of $\tilde{\mathbf{s}}^{(2)}$
0.7	10	0.225	30	0.001
0.7	20	0.224	30	0.001
5	20	0.366	50	0.001
10	20	0.578	75	0.003

Table 3.2: Parameters and RMSEs of the joint calibration and DoA estimation. DoAs are $-5°$, $0°$ and $5°$.

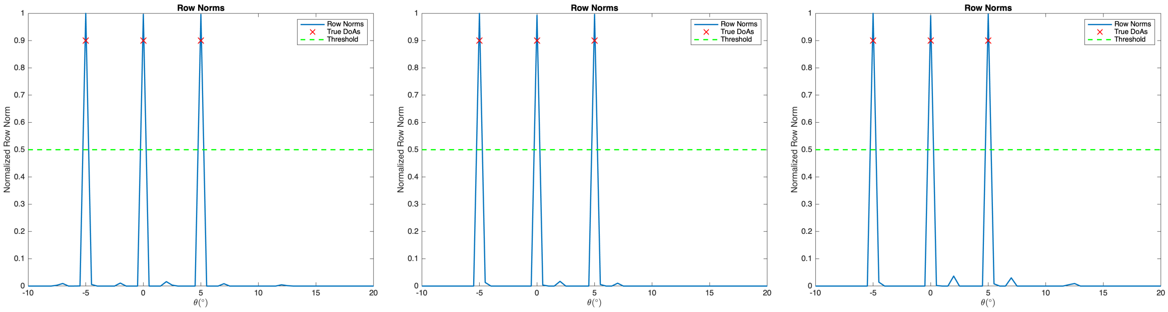

(a) Estimated row norms, $\sigma_{\text{inter}} = 20°$, $\sigma_{\text{intra}} = 0.7°$.

(b) Estimated row norms, $\sigma_{\text{inter}} = 20°$, $\sigma_{\text{intra}} = 5°$.

(c) Estimated row norms, $\sigma_{\text{inter}} = 20°$, $\sigma_{\text{intra}} = 10°$.

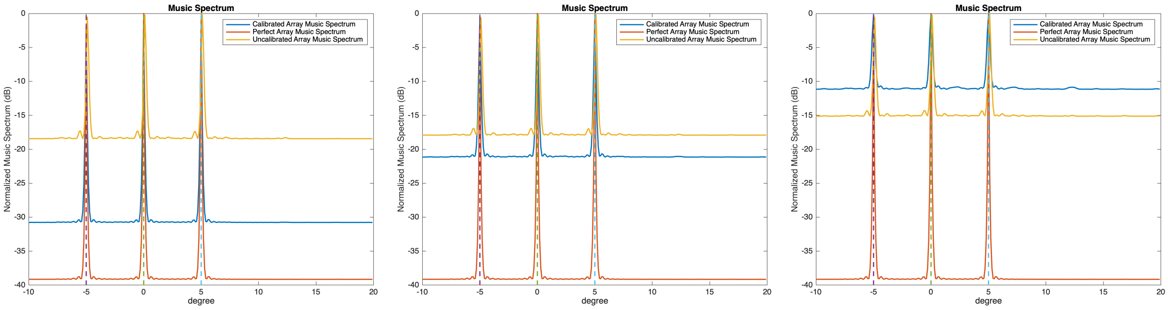

(d) MUSIC spectrum, $\sigma_{\text{inter}} = 20°$, $\sigma_{\text{intra}} = 0.7°$.

(e) MUSIC spectrum, $\sigma_{\text{inter}} = 20°$, $\sigma_{\text{intra}} = 5°$.

(f) MUSIC spectrum, $\sigma_{\text{inter}} = 20°$, $\sigma_{\text{intra}} = 10°$.

Figure 3.3: Estimated row norms and the MUSIC spectrum, DoAs are $-5°$, $0°$ and $5°$.

3.2 Step 2: Estimation Results

In this experiment, $M = N = 16$, $K = 2$, SNR $= 10dB$, and the target strengths are equal. The DoAs are fixed at $-5°$, $0°$, and $5°$, which are around the broadside. The proposed PAST-based approach is tested on 1000 measurements and compared with the one based on the EVD and the PAST-based MUSIC without the phase error estimation. Two combinations of the parameters for the varying phase error model are applied to the experiment: $\{\frac{\alpha}{\tau} = 0.02, \delta = 0.05\}$ and $\{\frac{\alpha}{\tau} = 0.2, \delta = 0.05\}$. At each iteration, a different realization of the phase errors is applied to generate a new measurement. The three above-mentioned methods use the same forgetting factor: $\beta_f = 0.995$ for the first parameter combination and $\beta_f = 0.99$ for the second. The threshold for selecting the peaks in (2.7) is 0.5. The RMSE of the phase error and DoA estimation at each iteration is calculated.

Figure 3.4 and Figure 3.5 show the results of the aforementioned methods. For the PAST-based MUSIC algorithm without the phase error estimation, the RMSEs of the phase errors are the errors between the true phase errors and the all-one vector. In Figure 3.4(a) and Figure 3.5(a), the phase errors are drawn from the model with $\{\alpha/\tau = 0.02,\ \delta = 0.05\}$. In Figure 3.4(b) and Figure 3.5(b), $\{\alpha/\tau = 0.2,\ \delta = 0.05\}$, which corresponds to larger phase error variations. In Figure 3.4(a), it can be observed that the PAST-based alternating method and the EVD-based one provide similar RMSEs of the phase error estimation. In Figure 3.4(b), with larger variations in the phase errors, the EVD-based alternating method provides slightly lower RMSEs of the phase error estimation. Moreover, it can be observed that for both parameter combinations, the RMSEs of the phase error estimation from the PAST-based alternating approach first increase to very high values at the very beginning of the iterations, and then immediately converge to lower values. This might be caused by the unsmoothness between the initial values and the values in the first few iterations for $\hat{\mathbf{U}}_s$ and $\mathbf{P}$ in (2.13). The initial values for $\hat{\mathbf{U}}_s$ and $\mathbf{P}$ are obtained from the estimated covariance matrix of the 10 measurements using the EVD, but the PAST algorithm directly updates the subspace with approximations. Therefore, the PAST loses track of the varying phase errors in the first few iterations. However, as more and more new measurements are utilized and those from the distant past are more and more down-weighted, the PAST returns to tracking the phase errors.

However, according to Figure 3.5, it seems that losing track of the phase errors does not have a dramatic influence on the DoA estimation for the PAST-based alternating method. For both parameter combinations, the PAST-based alternating update approach provides lower RMSEs for the DoA estimation with smaller variations, compared to those from the EVD-based method. Considering the computational cost decreased by using the PAST and that estimating the DoAs is more important, the PAST-based algorithm is preferable.

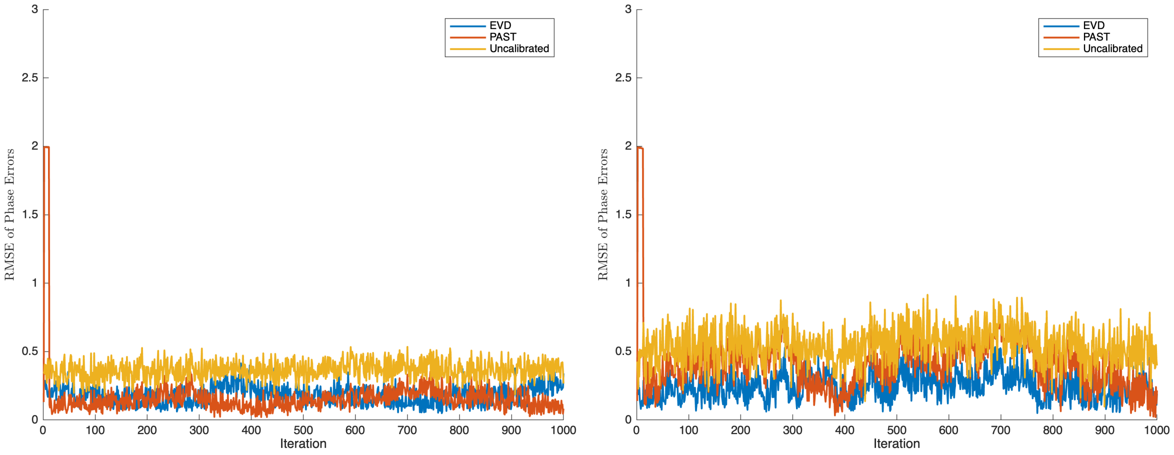

(a) RMSEs of the phase error estimation. $\alpha/\tau = 0.02$, $\delta = 0.05$ and $\beta_f = 0.995$.

(b) RMSEs of the phase error estimation. $\alpha/\tau = 0.2$, $\delta = 0.05$ and $\beta_f = 0.99$.

Figure 3.4: RMSEs of the phase error estimation from the PAST-based, the EVD-based alternating update approach, and the PAST-based MUSIC without the phase error estimation.

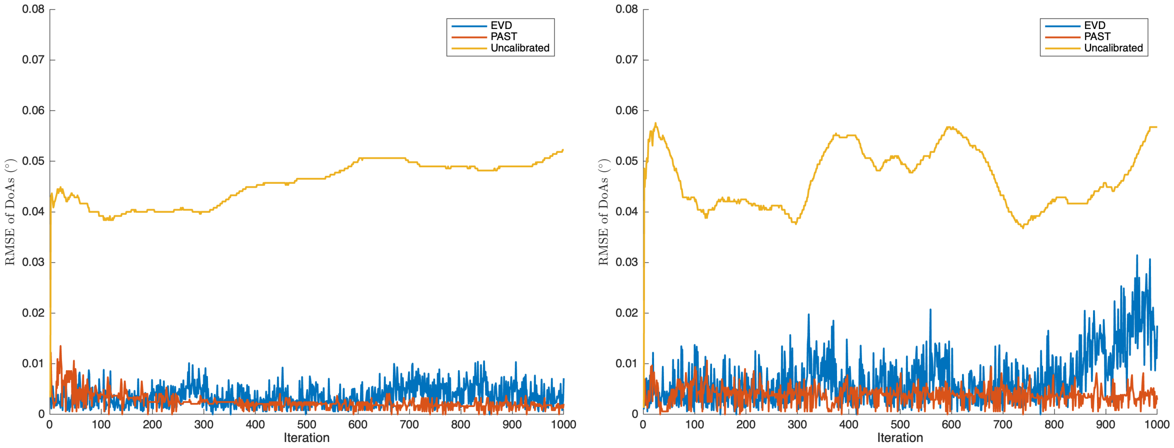

(a) RMSEs of the DoA estimation. $\alpha/\tau = 0.02$, $\delta = 0.05$ and $\beta_f = 0.995$.

(b) RMSEs of the DoA estimation. $\alpha/\tau = 0.2$, $\delta = 0.05$ and $\beta_f = 0.99$.

Figure 3.5: RMSEs of the DoA estimation from the PAST-based, the EVD-based alternating approach, and the PAST-based MUSIC without the phase error estimation.

3.3 Simulations of Beampatterns

In this experiment, the beampatterns of the calibrated array using the estimated phase errors from each step in the proposed approach are analyzed. The DoAs around the broadside, $-5°$, $0°$, and $5°$ are selected for conducting the proposed approach, and the SNR level is $10dB$ in the estimation procedure. The phase errors are the same as those in Figure 1.4. In the experiments related to the convex optimization, due to computational limits, only 40 simulations are performed; nevertheless, the results demonstrate that it is enough. As for the slowly varying phase error estimation, 1000 iterations are performed, and the estimated phase errors in each iteration are used to calibrate the phase errors in the current iteration.

Table 3.3 and Figure 3.6 show the comparison of the beampattern results. In Table 3.3, the mainlobe width, sidelobe levels, and the four highest peaking sidelobe levels of the beampatterns from the calibrated arrays with the corresponding approaches are also presented. In Figure 3.6(c), the convex optimization approach is applied to calibrate the phase errors in Figure 3.6(b), and in Figure 3.6(f), the alternating approach is used to calibrate the phase errors in Figure 3.6(e). It can be seen that all four highest peaking side lobes are suppressed to lower levels, and the sidelobe levels are suppressed to the same level as that of the array without the phase errors. Besides, the proposed approach does not introduce any influence on the mainlobe width. What is worth noticing is that the alternating approach provides beampatterns with lower peaking sidelobe levels than the convex optimization approach does, despite the one nearest to the mainlobe. This is consistent with the proposed methodology since the alternating approach aims at improving the initial estimates obtained from the convex optimization approach, whereas the convex optimization approach aims at reasonable initial estimates with only the prior information of target sparsity and die structure.

Phase Error Type	MW (°)	SL (dB)	PSL1 (dB)	PSL2 (dB)	PSL3 (dB)	PSL4 (dB)
No	0.67	-13.41	-54.13	-45.05	-49.24	-55.93
Static	0.67	-13.35	-22.51	-31.53	-35.23	-36.51
Slowly Varying	0.67	-13.06	-19.54	-29.05	-32.66	-34.45
Step 1 Calibrated	0.67	-13.39	-42.71	-47.44	-49.95	-50
Step 2 Calibrated	0.67	-13.41	-42.45	-50.73	-53.48	-52.01

Table 3.3: Average values of mainlobe width, sidelobe levels, and peaking sidelobe levels from the array without phase errors, with phase errors, and calibrated array.

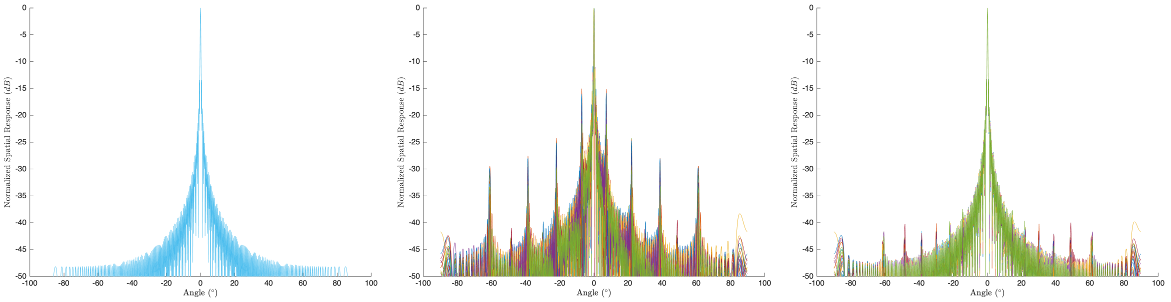

(a) Beampattern aiming at broadside without phase errors.

(b) Beampatterns on top of each other, aiming at broadside with 40 static phase error realizations.

(c) Beampatterns on top of each other, aiming at broadside after calibration.

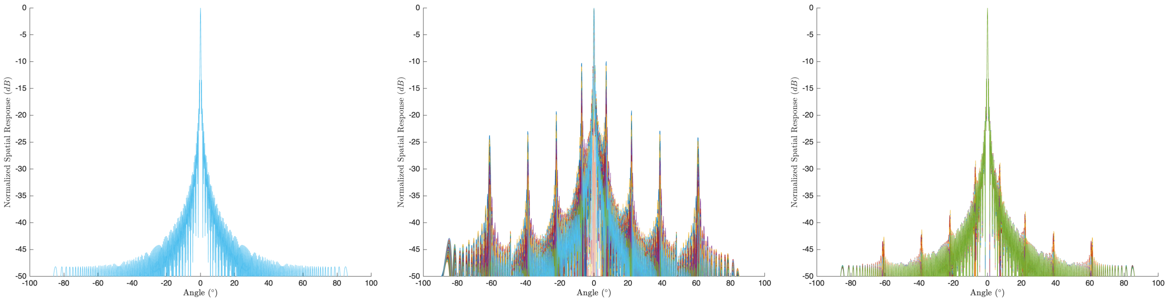

(d) Beampattern aiming at broadside without phase errors.

(e) Beampatterns on top of each other, aiming at broadside with 1000 slowly varying phase error realizations.

(f) Beampatterns on top of each other, aiming at broadside after calibration.

Figure 3.6: Beampatterns aiming at the broadside of the array without phase errors, uncalibrated, and calibrated array.

3.4 Dynamic Range Test

This experiment aims to test the proposed method in a scenario where the two targets are close to each other and have a dramatic difference between their SNR levels. The SNR levels for the two targets are set to $20dB$ and $0dB$, respectively. For the DoAs of the two targets, the $20dB$ target DoA is set to $0°$, and the $0dB$ one is set to $1.34°$, so that the angular difference is twice the $-3dB$ width of the mainlobe in Table 3.3.

For stage 1, 1000 realizations of the static phase errors are applied with $\sigma_{inter} = 10°$ and $\sigma_{intra} = 0.7°$. The RMSEs and the standard deviations of the DoA estimation from three array types are compared: (i) the perfect array (no phase error) using the MUSIC algorithm; (ii) uncalibrated array using MUSIC; and (iii) calibrated array using the die structure-based convex optimization approach, where the threshold for estimating the number of targets from the row norm peaks is set to 0.025 to adapt to the target with the lower SNR level and the regularization parameter is set to $\lambda = 30$. Besides, to avoid the huge computational time required by the convex optimization solver and the peak search in the MUSIC algorithm, the search field is limited around the two DoAs, i.e., between $-0.1°$ and $0.1°$, and between $1.1°$ and $1.5°$, with a search grid width of

0.001°.

Table 3.4 presents the RMSEs and the standard deviations of the three types of processing mentioned above. It can be observed that the uncalibrated array generates the highest RMSEs and standard deviations for both targets. Besides, the estimation performance of the target with the higher SNR level is worse and less stable, where larger values of the RMSE and standard deviation than those of target 2 can be observed. This means that under the setting in this dynamic range test, the phase errors have a larger influence on the performance of the MUSIC algorithm related to the target with a higher SNR level.

The perfect array provides the best results, where the lowest RMSEs and zero-value standard deviations for both targets can be observed. These results illustrate the best performance that the MUSIC algorithm can achieve without phase errors in this setting.

The values of the RMSE and standard deviation of both targets from the proposed approach are much lower than those from the other two types of array, and they are close to those of the perfect array. These results demonstrate the effectiveness of the proposed approach. Although the phase errors cannot be perfectly estimated, the estimates of the number of targets and the phase errors from the proposed approach are sufficient for calibrating the antennas and conducting the MUSIC algorithm.

	Target 1, $20dB$		Target 2, $0dB$	
Array Type	RMSE (°)	Standard Deviation (°)	RMSE (°)	Standard Deviation (°)
Perfect Array	0.0010	0	0.0020	0
Uncalibrated	0.0208	0.0162	0.0206	0.0160
Calibrated	0.0014	0.0011	0.0021	0.0014

Table 3.4: RMSE and standard deviation of the DoA estimation for dynamic range test with static phase errors.

For stage 2, 1000 realizations of the slowly varying phase errors are drawn with $\frac{\alpha}{\tau} = 0.02$ and $\delta = 0.05$. In each iteration, a different realization of the phase errors is applied to generate a new measurement. The RMSEs of the phase error and DoA estimation from the PAST-based alternating update approach, the one based on the EVD, and the PAST-based MUSIC without the phase error estimation are calculated and compared. The forgetting factors are 0.99 for the three algorithms. The search field is limited around the two DoAs, i.e., between $-0.4°$ and $0.4°$, and between $0.9°$ and $1.6°$, with a search grid width of $0.001°$.

Figure 3.7 illustrates the estimation results from the three aforementioned methods. The RMSEs for the uncalibrated array are the errors between the true phase errors and the all-one vector. It can be seen that the results from the EVD-based alternating update approach cannot converge. Note here that different values of the forgetting factor are applied to the EVD-based method, but the results are more or less the same, and hence the results with the same β_f as the other two methods are shown as an illustration. In Figure 3.7(c), it can be observed that the RMSEs of the phase error estimation from the PAST-based algorithm first show high values but gradually converge to stable values, which are lower than those from the uncalibrated array. By contrast, although the RMSEs of the phase error estimation from the EVD-based one do not show dramatically high values in the first few iterations, with the phase errors varying, they begin diverging and show higher values than those from the PAST-based one throughout the iterations. In Figure 3.7(a) and Figure 3.7(b), it can be observed that the RMSE values of the DoA estimation from the PAST-based algorithm after around 500 iterations are much lower than those from the EVD-based one and the uncalibrated array, despite the relatively higher values appearing only at the beginning of the iterations.

What is worth noticing is that for both the PAST and the EVD-based algorithm, the trends of the RMSE values of the phase error and the DoA estimation over iterations are very similar, comparing Figure 3.7(c) with Figure 3.7(a) and Figure 3.7(b). This implies the consistency between the antenna calibration and the DoA estimation in the proposed approach. Since both algorithms iteratively update the DoAs and phase errors based on each other, inaccuracies in phase error estimates can propagate and degrade the DoA estimation, and vice versa. Nevertheless, the return to the low RMSEs demonstrates the adaptability of the proposed approach to the varying phase errors and the effectiveness of accurately estimating two closely spaced targets with a dramatic SNR level difference.

To better observe the RMSE values of the DoA estimation for the two targets from the PAST-based alternating approach, the values after 500 iterations are shown in Figure 3.7(d). It can be observed that the RMSEs for the estimation of the $0dB$ target are, in general, higher than those of the $20dB$ target. Also, compared to Figure 3.7(a), the RMSEs from the EVD and PAST-based alternating method in Figure 3.7(b) exhibit more local fluctuations. These observations indicate reduced accuracy and stability of the DoA estimation for the lower SNR target.

Although the PAST-based alternating update approach shows better stability and higher accuracy in estimating the DoAs with 1000 iterations in this dynamic range test, it does not mean that this approach is always a better option. If the varying stage lasts very short, e.g., within 100 radar cycles, then obviously the EVD-based alternating approach provides higher accuracy for the DoA estimation in this dynamic range test. Besides, in Figure 3.5(a) and Figure 3.5(b) shown in Section 3.2, the RMSEs of the DoA estimation have demonstrated that the EVD-based method provides reasonable accuracy. Hence, if the computational cost is acceptable, the EVD-based alternating approach should be preferred when the varying stage is within 100 radar cycles.

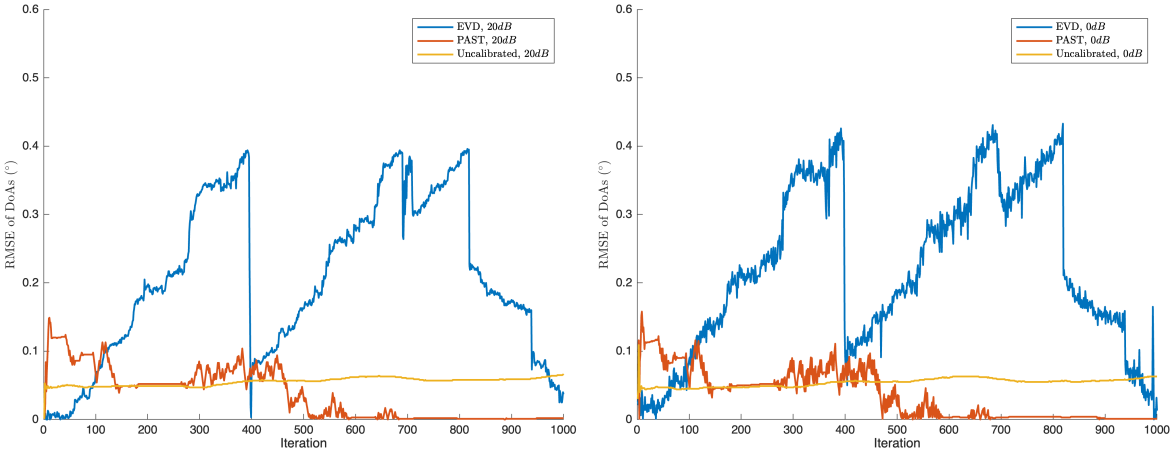

(a) RMSEs of the DoA estimation for the $20dB$ target.

(b) RMSEs of the DoA estimation for the $0dB$ target.

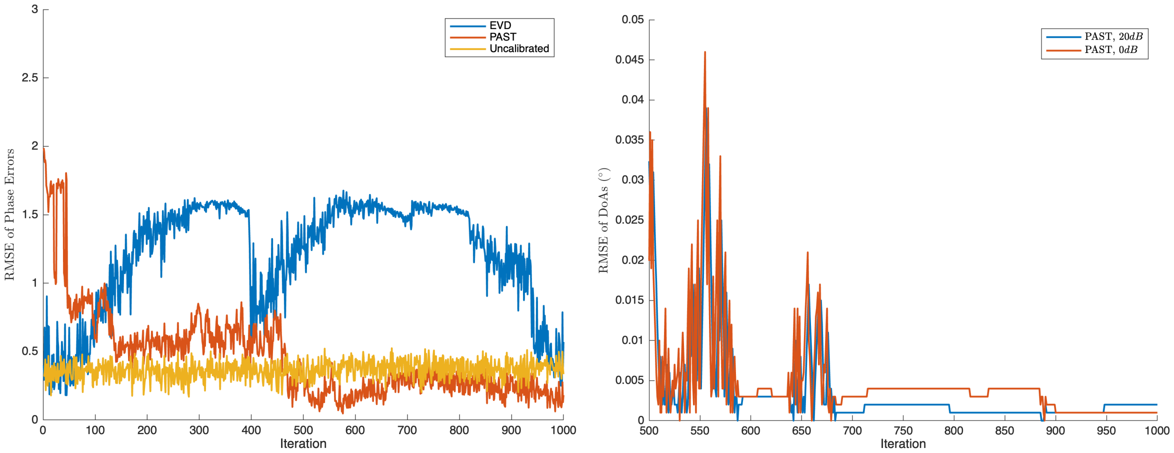

(c) RMSEs of the phase error estimation.

(d) RMSEs of the DoA estimation from the PAST-based alternating method after 500 iterations.

Figure 3.7: RMSE of the slowly varying phase error and DoA estimation for dynamic range test. The SNR levels for target 1 and target 2 are $20dB$ and $0dB$, respectively.

3.5 Conclusions

This chapter evaluated the effectiveness of the proposed two-step approach through comprehensive simulations. In the static stage, the die structure-based convex optimization method was shown to provide reliable initial estimates of the inter-die phase errors and DoAs. In the varying stage, the PAST-based alternating update algorithm successfully tracked both the varying phase errors and the DoAs, achieving comparable or improved performance over the EVD-based one, with reduced computational complexity. Beampattern simulations illustrated that both steps significantly suppress peaking sidelobes without worsening the angular resolution. Furthermore, the dynamic range test confirmed the robustness of the proposed method when targets have drastically different SNR levels.

Cramér-Rao Bound Derivation

4

In this Chapter, the CRB incorporating the phase errors and the DoAs is derived from Bangs' formula [20] with information in the mean and covariance of the measurements [21]. Section 4.1 first derives the Fisher information matrix of the DoAs based on more general assumptions on the reflection coefficients considering deterministic and unknown phase errors, and then analyzes the mean and covariance information, respectively, revealing the mathematical relation between two different assumptions on the reflection coefficients: $\mathbf{s}(t)$ is deterministic, unknown and changes over time, or it is spatially white Gaussian. Section 4.2 focuses on the derivation of the CRB for both phase errors and DoAs based on the deterministic and unknown $\mathbf{s}(t)$ and $\boldsymbol{\gamma}$, which is chosen as the key assumption for this thesis.

4.1 Fisher Information

Although the reflection coefficients $\mathbf{s}(t)$ are not the parameters of interest in this thesis, the CRB is dependent on them, and hence, appropriate assumptions for $\mathbf{s}(t)$ are required. Since $\mathbf{s}(t)$ changes over time, multiple measurements are collected and the CRB can be analyzed based on the mean and the covariance matrix of $\mathbf{s}(t)$. To do so, it is assumed that the phase errors remain unchanged during those collected measurements. Hence, the corresponding signal model is given by (1.9):

$$\mathbf{X} = \boldsymbol{\Gamma}\mathbf{A}\mathbf{S} + \mathbf{N}. \tag{4.1}$$

Assuming the D Gaussian reflection coefficients at time t, $\mathbf{s}(t) \sim \mathcal{CN}(\boldsymbol{\mu}_s(t), \boldsymbol{\Sigma}_s)$, and the noise $\mathbf{n}(t) \sim \mathcal{CN}(\mathbf{0}_M, \sigma_n^2\mathbf{I}_M)$, according to the Bangs' formula [20], the elements of the Fisher information matrix corresponding to $\boldsymbol{\omega}$ at time index t are:

$$[\mathbf{F}_{\boldsymbol{\omega}\boldsymbol{\omega}}(t)]_{i,j} = F_{\omega_i\omega_j}(t) = 2\mathrm{Re}\{\frac{\partial \boldsymbol{\mu}_x^H(t)}{\partial \omega_i}\mathbf{C}_x^{-1}\frac{\partial \boldsymbol{\mu}_x(t)}{\partial \omega_j}\} + \mathrm{Tr}(\mathbf{C}_x^{-1}\frac{\partial \mathbf{C}_x^{-1}}{\partial \omega_i}\mathbf{C}_x^{-1}\frac{\partial \mathbf{C}_x^{-1}}{\partial \omega_j}), \tag{4.2}$$

where

$$\begin{aligned} \boldsymbol{\omega} &= [\omega_1, \omega_2, \ldots, \omega_D]^T, \\ \omega_d &= 2\pi \sin\theta_d, \\ \boldsymbol{\mu}_x(t) &= \mathrm{E}[\mathbf{x}(t)] = \boldsymbol{\Gamma}\mathbf{A}\boldsymbol{\mu}_s(t), \\ \mathbf{C}_x &= \mathrm{E}\{[\mathbf{x}(t) - \mathrm{E}\mathbf{x}(t)][\mathbf{x}(t) - \mathrm{E}\mathbf{x}(t)]^H\} \\ &= \boldsymbol{\Gamma}\mathbf{A}\boldsymbol{\Sigma}_s\mathbf{A}^H\boldsymbol{\Gamma}^H + \sigma_n^2\mathbf{I}. \end{aligned} \tag{4.3}$$

Besides, by vectorizing $\mathbf{C}_x$, one can obtain:

$$\mathbf{c}_x = \mathrm{vec}(\mathbf{C}_x) = (\overline{\boldsymbol{\Gamma}\mathbf{A}} \circ \boldsymbol{\Gamma}\mathbf{A})\mathrm{diag}(\boldsymbol{\Sigma}_s) + \mathrm{vec}(\mathbf{I})\sigma_n^2, \tag{4.4}$$

which will be useful later on.

Denote

$$\begin{aligned} B^{(1)}_{\omega_i\omega_j}(t) &= 2\text{Re}\{\frac{\partial \boldsymbol{\mu}^H_x(t)}{\partial \omega_i}\mathbf{C}_x^{-1}\frac{\partial \boldsymbol{\mu}_x(t)}{\partial \omega_j}\}, \\ B^{(2)}_{\omega_i\omega_j}(t) &= \text{Tr}(\mathbf{C}_x^{-1}\frac{\partial \mathbf{C}_x^{-1}}{\partial \omega_i}\mathbf{C}_x^{-1}\frac{\partial \mathbf{C}_x^{-1}}{\partial \omega_j}), \end{aligned} \tag{4.5}$$

where $B^{(1)}_{\omega_i\omega_j}(t)$ and $B^{(2)}_{\omega_i\omega_j}(t)$ correspond to the information in the mean and covariance, respectively. Note that $F_{\omega_i\omega_j}(t) = B^{(1)}_{\omega_i\omega_j}(t) + B^{(2)}_{\omega_i\omega_j}(t)$.

Before further derivation, introduce the notations

$$\begin{aligned} \mathbf{D}(\boldsymbol{\omega}) &= [\mathbf{d}(\omega_1), \mathbf{d}(\omega_2), \ldots, \mathbf{d}(\omega_d)], \\ \mathbf{d}(\omega_i) &= \frac{\partial \mathbf{a}(\omega_i)}{\partial \omega_i}, \\ \bar{\mathbf{D}}(\boldsymbol{\omega}) &= [\bar{\mathbf{d}}(\omega_1), \bar{\mathbf{d}}(\omega_2), \ldots, \bar{\mathbf{d}}(\omega_d)], \\ \bar{\mathbf{d}}(\omega_i) &= \frac{\partial \bar{\mathbf{a}}(\omega_i)}{\partial \omega_i}. \end{aligned} \tag{4.6}$$

Then, based on (4.2)-(4.5), the terms of the Fisher information corresponding to the mean and covariance are respectively given by:

$$B^{(1)}_{\omega_i\omega_j}(t) = 2\text{Re}\{\mathbf{d}^H(\omega_i)\boldsymbol{\Gamma}^H\mathbf{C}_x^{-1}\boldsymbol{\Gamma}\mathbf{d}(\omega_j) \cdot \mu^*_{si}(t)\mu_{sj}(t)\}, \tag{4.7}$$

$$B^{(2)}_{\omega_i\omega_j}(t) = \mathbf{j}_i^H(\bar{\mathbf{C}}_x^{-1} \otimes \mathbf{C}_x^{-1})\mathbf{j}_j, \tag{4.8}$$

where $\mathbf{j}_i$ is the Jacobian obtained by evaluating the gradient of vec($\mathbf{C}_x$) w.r.t ω_i:

$$\begin{aligned} \mathbf{j}(\omega_i) &= \frac{\partial \text{vec}(\mathbf{C}_x)}{\partial \omega_i} \\ &= \frac{\partial \mathbf{c}_x}{\partial \omega_i} \\ &= \sigma^2_{si}[\overline{\boldsymbol{\Gamma}\mathbf{a}}(\omega_i) \circ \boldsymbol{\Gamma}\mathbf{d}(\omega_i) + \overline{\boldsymbol{\Gamma}\mathbf{d}}(\omega_i) \circ \boldsymbol{\Gamma}\mathbf{a}(\omega_i)], \end{aligned} \tag{4.9}$$

with σ^2_{si} the ith element on the diagonal of $\boldsymbol{\Sigma}_s$.

4.1.1 Mean Information

For notational convenience, first define:

$$\begin{aligned} \mathbf{D}_{\boldsymbol{\Gamma}} &= \boldsymbol{\Gamma}\mathbf{D}, \\ \mathbf{A}_{\boldsymbol{\Gamma}} &= \boldsymbol{\Gamma}\mathbf{A}, \end{aligned} \tag{4.10}$$

where $\mathbf{A} = \mathbf{A}(\boldsymbol{\omega})$ and $\mathbf{D} = \mathbf{D}(\boldsymbol{\omega})$. According to (4.3), (4.7) can be written as:

$$B^{(1)}_{\omega_i\omega_j}(t) = 2\text{Re}\{\mathbf{d}^H_{\boldsymbol{\Gamma}}(\omega_i)(\sigma_n^2\mathbf{I} + \mathbf{A}_{\boldsymbol{\Gamma}}\boldsymbol{\Sigma}_s\mathbf{A}^H_{\boldsymbol{\Gamma}})^{-1}\mathbf{d}_{\boldsymbol{\Gamma}}(\omega_j) \cdot \mu^*_{si}(t)\mu_{sj}(t)\}. \tag{4.11}$$

and by applying the matrix inversion lemma on $\mathbf{C}_x$:

$$\begin{aligned}\mathbf{C}_x^{-1} &= (\sigma_n^2\mathbf{I} + \mathbf{A}_{\boldsymbol{\Gamma}}\boldsymbol{\Sigma}_s\mathbf{A}_{\boldsymbol{\Gamma}}^H)^{-1} \\ &= \frac{1}{\sigma_n^2}[\mathbf{I} - \mathbf{A}_{\boldsymbol{\Gamma}}(\sigma_n^2\boldsymbol{\Sigma}_s^{-1} + \mathbf{A}_{\boldsymbol{\Gamma}}^H\mathbf{A}_{\boldsymbol{\Gamma}})^{-1}\mathbf{A}_{\boldsymbol{\Gamma}}^H],\end{aligned} \tag{4.12}$$

(4.11) becomes:

$$B^{(1)}_{\omega_i\omega_j}(t) = \frac{2}{\sigma_n^2}\mathrm{Re}\{\mathbf{d}_{\boldsymbol{\Gamma}}(\omega_i)^H[\mathbf{I} - \mathbf{A}_{\boldsymbol{\Gamma}}(\sigma_n^2\boldsymbol{\Sigma}_s^{-1} + \mathbf{A}_{\boldsymbol{\Gamma}}^H\mathbf{A}_{\boldsymbol{\Gamma}})^{-1}\mathbf{A}_{\boldsymbol{\Gamma}}^H]\mathbf{d}_{\boldsymbol{\Gamma}}(\omega_j) \cdot \mu_{si}^*(t)\mu_{sj}(t)\}. \tag{4.13}$$

Hence, the term of the Fisher information matrix related to the mean is:

$$\mathbf{B}^{(1)}_{\boldsymbol{\omega\omega}}(t) = \frac{2}{\sigma_n^2}\mathrm{Re}\{\mathbf{D}_{\boldsymbol{\Gamma}}^H[\mathbf{I} - \mathbf{A}_{\boldsymbol{\Gamma}}(\sigma_n^2\boldsymbol{\Sigma}_s^{-1} + \mathbf{A}_{\boldsymbol{\Gamma}}^H\mathbf{A}_{\boldsymbol{\Gamma}})^{-1}\mathbf{A}_{\boldsymbol{\Gamma}}^H]\mathbf{D}_{\boldsymbol{\Gamma}} \odot \boldsymbol{\Lambda}_s^T(t)\}, \tag{4.14}$$

where $\boldsymbol{\Lambda}_s^T(t) = \bar{\boldsymbol{\mu}}_s(t)\boldsymbol{\mu}_s^T(t)$ and $\boldsymbol{\Lambda}_s(t) = \boldsymbol{\mu}_s(t)\boldsymbol{\mu}_s^H(t)$.

When $\mathbf{s}(t)$ is considered to be deterministic, unknown, and changing over time, the mean of $\mathbf{s}(t)$ at time index t can be set to the variable itself, i.e., $\boldsymbol{\mu}_s(t) = \mathbf{s}(t)$, and there is no covariance information for $\mathbf{s}(t)$ since it is not statistical. Hence, $B^{(2)}_{\omega_i\omega_j}(t)$ vanishes and in (4.14), $\boldsymbol{\Sigma}_s$ vanishes and $\boldsymbol{\Lambda}_s^T(t)$ is replaced by $\bar{\mathbf{s}}(t)\mathbf{s}(t)^T$. Based on these observations and collecting T measurements, the Fisher information matrix corresponding to $\boldsymbol{\omega}$ is therefore given by:

$$\begin{aligned}\mathbf{F}^{(1)}_{\boldsymbol{\omega\omega}} &= \sum_{t=0}^{T-1}\frac{2}{\sigma_n^2}\mathrm{Re}\{\mathbf{D}_{\boldsymbol{\Gamma}}^H[\mathbf{I} - \mathbf{A}_{\boldsymbol{\Gamma}}(\mathbf{A}_{\boldsymbol{\Gamma}}^H\mathbf{A}_{\boldsymbol{\Gamma}})^{-1}\mathbf{A}_{\boldsymbol{\Gamma}}^H]\mathbf{D}_{\boldsymbol{\Gamma}} \odot [\bar{\mathbf{s}}(t)\mathbf{s}^T(t)]\} \\ &= \frac{2T}{\sigma_n^2}\mathrm{Re}\{\mathbf{D}_{\boldsymbol{\Gamma}}^H[\mathbf{I} - \mathbf{A}_{\boldsymbol{\Gamma}}(\mathbf{A}_{\boldsymbol{\Gamma}}^H\mathbf{A}_{\boldsymbol{\Gamma}})^{-1}\mathbf{A}_{\boldsymbol{\Gamma}}^H]\mathbf{D}_{\boldsymbol{\Gamma}} \odot [\frac{1}{T}\sum_{t=0}^{T-1}\bar{\mathbf{s}}(t)\mathbf{s}^T(t)]\} \\ &= \frac{2T}{\sigma_n^2}\mathrm{Re}\{\mathbf{D}_{\boldsymbol{\Gamma}}^H[\mathbf{I} - \mathbf{A}_{\boldsymbol{\Gamma}}(\mathbf{A}_{\boldsymbol{\Gamma}}^H\mathbf{A}_{\boldsymbol{\Gamma}})^{-1}\mathbf{A}_{\boldsymbol{\Gamma}}^H]\mathbf{D}_{\boldsymbol{\Gamma}} \odot \mathbf{R}_s^T\}.\end{aligned} \tag{4.15}$$

where $\mathbf{R}_s = \mathbf{S}\mathbf{S}^H/T$. Besides, because the matrix of the phase error is always unitary such that $\boldsymbol{\Gamma}\boldsymbol{\Gamma}^H = \boldsymbol{\Gamma}^H\boldsymbol{\Gamma} = \mathbf{I}_{NM}$, (4.15) can be further expressed as:

$$\begin{aligned}\mathbf{F}^{(1)}_{\boldsymbol{\omega\omega}} &= \frac{2T}{\sigma_n^2}\mathrm{Re}\{\mathbf{D}_{\boldsymbol{\Gamma}}^H[\mathbf{I} - \mathbf{A}_{\boldsymbol{\Gamma}}(\mathbf{A}_{\boldsymbol{\Gamma}}^H\mathbf{A}_{\boldsymbol{\Gamma}})^{-1}\mathbf{A}_{\boldsymbol{\Gamma}}^H]\mathbf{D}_{\boldsymbol{\Gamma}} \odot \mathbf{R}_s^T\} \\ &= \frac{2T}{\sigma_n^2}\mathrm{Re}\{\mathbf{D}^H[\mathbf{I} - \mathbf{A}(\mathbf{A}^H\mathbf{A})^{-1}\mathbf{A}^H]\mathbf{D} \ \odot \mathbf{R}_s^T\}.\end{aligned} \tag{4.16}$$

Hence, it is independent of the phase errors and is identical to the expression in the work of [15–17] with the same assumption for $\mathbf{s}(t)$. This is intuitive since the phase errors are assumed to be known for this derivation.

Instead of $\boldsymbol{\omega}$, in this thesis, $\boldsymbol{\theta}$ is the parameter of interest. The Fisher information with respect to $\boldsymbol{\theta}$ can be easily derived and is given by:

$$\mathbf{F}^{(1)}_{\boldsymbol{\theta\theta}} = \boldsymbol{\Psi}_{\boldsymbol{\theta}}\mathbf{F}^{(1)}_{\boldsymbol{\omega\omega}}\boldsymbol{\Psi}_{\boldsymbol{\theta}}, \tag{4.17}$$

where $\mathbf{\Psi}_{\boldsymbol{\theta}}$ is a diagonal matrix with the ith element on the diagonal being [22]:

$$[\mathbf{\Psi}_{\boldsymbol{\theta}}]_{ii} = \frac{d\omega_i}{d\theta_i} = 2\pi \cos \theta_i. \tag{4.18}$$

4.1.2 Covariance Information

According to (4.8) and (4.9), the term of the Fisher information matrix related to the covariance is:

$$\mathbf{B}^{(2)}_{\boldsymbol{\omega}\boldsymbol{\omega}}(t) = \mathbf{J}^H(\boldsymbol{\omega})(\bar{\mathbf{C}}_x^{-1} \otimes \mathbf{C}_x^{-1})\mathbf{J}(\boldsymbol{\omega}), \tag{4.19}$$

which can also be written as:

$$\mathbf{B}^{(2)}_{\boldsymbol{\omega}\boldsymbol{\omega}}(t) = \mathbf{J}^H(\boldsymbol{\omega})(\bar{\mathbf{C}}_x \otimes \mathbf{C}_x)^{-1}\mathbf{J}(\boldsymbol{\omega}). \tag{4.20}$$

Here $\mathbf{J}(\boldsymbol{\omega}) = [\mathbf{j}(\omega_1), \mathbf{j}(\omega_2), \ldots, \mathbf{j}(\omega_D)]$, which can be expressed as:

$$\mathbf{J}(\boldsymbol{\omega}) = \frac{\partial \mathbf{c}_x}{\partial \boldsymbol{\omega}^T} = [\bar{\mathbf{A}}_{\mathbf{\Gamma}} \circ \mathbf{D}_{\mathbf{\Gamma}} + \bar{\mathbf{D}}_{\mathbf{\Gamma}} \circ \mathbf{A}_{\mathbf{\Gamma}}]\mathbf{\Sigma}_s. \tag{4.21}$$

When $\mathbf{s}(t)$ is considered to be zero mean spatially white Gaussian, the part corresponding to $B^{(1)}_{\omega_i\omega_j}(t)$ vanishes. Hence, the Fisher information matrix corresponding to $\boldsymbol{\omega}$ at time index t is just $\mathbf{B}^{(2)}_{\boldsymbol{\omega}\boldsymbol{\omega}}(t)$, and with T measurements, the Fisher information matrix is given by:

$$\mathbf{F}^{(2)}_{\boldsymbol{\omega}\boldsymbol{\omega}} = \sum_{t=0}^{T-1} \mathbf{B}^{(2)}_{\boldsymbol{\omega}\boldsymbol{\omega}}(t) = T\mathbf{B}^{(2)}_{\boldsymbol{\omega}\boldsymbol{\omega}}(0), \tag{4.22}$$

which is also shown in the previous work [11,13,14] under the zero mean spatially white Gaussian assumption.

Similar to (4.17), the Fisher information matrix with respect to $\boldsymbol{\theta}$ in this case is:

$$\mathbf{F}^{(2)}_{\boldsymbol{\theta}\boldsymbol{\theta}} = \mathbf{\Psi}_{\boldsymbol{\theta}}\mathbf{F}^{(2)}_{\boldsymbol{\omega}\boldsymbol{\omega}}\mathbf{\Psi}_{\boldsymbol{\theta}}. \tag{4.23}$$

4.2 CRB for Deterministic and Unknown Parameters

The zero mean spatially white Gaussian assumption provides a simple and effective model for the reflection coefficients $\mathbf{s}(t)$, but in reality, these reflection coefficients are usually not white Gaussian. In contrast, assuming $\mathbf{s}(t)$ is deterministic, unknown, and changing over time can cover the time-varying characteristics of $\mathbf{s}(t)$ without restricting it to a specific distribution. Besides, (4.17) explicitly shows the effect of environmental noise variance σ_n^2 comparing it to (4.23). Hence, in this thesis, the assumption that $\mathbf{s}(t)$ is deterministic, unknown, and changing over time is chosen. Therefore, the Fisher information matrix of $\boldsymbol{\theta}$ for T measurements is given by:

$$\mathbf{F}_{\boldsymbol{\theta}\boldsymbol{\theta}} = \frac{2T}{\sigma_n^2}\mathrm{Re}\{\mathbf{\Psi}_{\boldsymbol{\theta}}\mathbf{D}^H[\mathbf{I} - \mathbf{A}(\mathbf{A}^H\mathbf{A})^{-1}\mathbf{A}^H]\mathbf{D}\mathbf{\Psi}_{\boldsymbol{\theta}} \odot \mathbf{R}_s^T\}. \tag{4.24}$$

For the Fisher information matrix corresponding to $\boldsymbol{\gamma}$, we first derive the mean with respect to $\boldsymbol{\gamma}$ for a single measurement at time index t:

$$\frac{\partial \boldsymbol{\mu}_x(t)}{\partial \boldsymbol{\gamma}} = \mathrm{diag}(\mathbf{A}\mathbf{s}(t)). \tag{4.25}$$

Then, by replacing $\frac{\partial \boldsymbol{\mu}_x(t)}{\partial \boldsymbol{\omega}}$ with $\frac{\partial \boldsymbol{\mu}_x(t)}{\partial \boldsymbol{\gamma}}$, the Fisher information corresponding to $\boldsymbol{\gamma}$ for a single measurement becomes:

$$\begin{aligned}
\mathbf{F}_{\boldsymbol{\gamma}\boldsymbol{\gamma}}(t) &= \frac{2}{\sigma_n^2}\mathrm{Re}\{\mathrm{diag}(\overline{\mathbf{A}\mathbf{s}}(t))[\mathbf{I} - \mathbf{A}_{\boldsymbol{\Gamma}}(\mathbf{A}_{\boldsymbol{\Gamma}}^H\mathbf{A}_{\boldsymbol{\Gamma}})^{-1}\mathbf{A}_{\boldsymbol{\Gamma}}^H]\mathrm{diag}(\mathbf{A}\mathbf{s}(t))\} \\
&= \frac{2}{\sigma_n^2}\mathrm{Re}\{[\mathbf{I} - \mathbf{A}_{\boldsymbol{\Gamma}}(\mathbf{A}_{\boldsymbol{\Gamma}}^H\mathbf{A}_{\boldsymbol{\Gamma}})^{-1}\mathbf{A}_{\boldsymbol{\Gamma}}^H] \odot [\overline{\mathbf{A}\mathbf{s}}(t)(\mathbf{A}\mathbf{s}^T(t))]\} \\
&= \frac{2}{\sigma_n^2}\mathrm{Re}\{[\mathbf{I} - \mathbf{A}_{\boldsymbol{\Gamma}}(\mathbf{A}_{\boldsymbol{\Gamma}}^H\mathbf{A}_{\boldsymbol{\Gamma}})^{-1}\mathbf{A}_{\boldsymbol{\Gamma}}^H] \odot [\bar{\mathbf{A}}\bar{\mathbf{s}}(t)\mathbf{s}^T(t)\mathbf{A}^T]\}.
\end{aligned} \tag{4.26}$$

For T measurements, we obtain:

$$\begin{aligned}
\mathbf{F}_{\boldsymbol{\gamma}\boldsymbol{\gamma}} &= \sum_{t=0}^{T-1}\frac{2}{\sigma_n^2}\mathrm{Re}\{[\mathbf{I} - \mathbf{A}_{\boldsymbol{\Gamma}}(\mathbf{A}_{\boldsymbol{\Gamma}}^H\mathbf{A}_{\boldsymbol{\Gamma}})^{-1}\mathbf{A}_{\boldsymbol{\Gamma}}^H] \odot [\bar{\mathbf{A}}\bar{\mathbf{s}}(t)\mathbf{s}^T(t)\mathbf{A}^T]\} \\
&= \frac{2T}{\sigma_n^2}\mathrm{Re}\{[\mathbf{I} - \mathbf{A}_{\boldsymbol{\Gamma}}(\mathbf{A}_{\boldsymbol{\Gamma}}^H\mathbf{A}_{\boldsymbol{\Gamma}})^{-1}\mathbf{A}_{\boldsymbol{\Gamma}}^H] \odot [\bar{\mathbf{A}}\frac{1}{T}\sum_{t=0}^{T-1}(\bar{\mathbf{s}}(t)\mathbf{s}^T(t))\mathbf{A}^T]\} \\
&= \frac{2T}{\sigma_n^2}\mathrm{Re}\{[\mathbf{I} - \mathbf{A}_{\boldsymbol{\Gamma}}(\mathbf{A}_{\boldsymbol{\Gamma}}^H\mathbf{A}_{\boldsymbol{\Gamma}})^{-1}\mathbf{A}_{\boldsymbol{\Gamma}}^H] \odot [\bar{\mathbf{A}}\mathbf{R}_s^T\mathbf{A}^T]\}.
\end{aligned} \tag{4.27}$$

Similarly, the Fisher information corresponding to $\boldsymbol{\theta}$ and $\boldsymbol{\gamma}$ can also be derived, which is:

$$\begin{aligned}
\mathbf{F}_{\boldsymbol{\theta}\boldsymbol{\gamma}}(t) &= \frac{2}{\sigma_n^2}\mathrm{Re}\{\mathrm{diag}(\bar{\mathbf{s}}(t))\boldsymbol{\Psi}_{\boldsymbol{\theta}}\mathbf{D}_{\boldsymbol{\Gamma}}^H[\mathbf{I} - \mathbf{A}_{\boldsymbol{\Gamma}}(\mathbf{A}_{\boldsymbol{\Gamma}}^H\mathbf{A}_{\boldsymbol{\Gamma}})^{-1}\mathbf{A}_{\boldsymbol{\Gamma}}^H]\mathrm{diag}(\mathbf{A}\mathbf{s}(t))\} \\
&= \frac{2}{\sigma_n^2}\mathrm{Re}\{\boldsymbol{\Psi}_{\boldsymbol{\theta}}\mathbf{D}_{\boldsymbol{\Gamma}}^H[\mathbf{I} - \mathbf{A}_{\boldsymbol{\Gamma}}(\mathbf{A}_{\boldsymbol{\Gamma}}^H\mathbf{A}_{\boldsymbol{\Gamma}})^{-1}\mathbf{A}_{\boldsymbol{\Gamma}}^H] \odot [\bar{\mathbf{s}}(t)(\mathbf{A}\mathbf{s}(t))^T]\} \\
&= \frac{2}{\sigma_n^2}\mathrm{Re}\{\boldsymbol{\Psi}_{\boldsymbol{\theta}}\mathbf{D}_{\boldsymbol{\Gamma}}^H[\mathbf{I} - \mathbf{A}_{\boldsymbol{\Gamma}}(\mathbf{A}_{\boldsymbol{\Gamma}}^H\mathbf{A}_{\boldsymbol{\Gamma}})^{-1}\mathbf{A}_{\boldsymbol{\Gamma}}^H] \odot [\bar{\mathbf{s}}(t)\mathbf{s}^T(t)\mathbf{A}^T]\},
\end{aligned} \tag{4.28}$$

and for T measurements it is:

$$\begin{aligned}
\mathbf{F}_{\boldsymbol{\theta}\boldsymbol{\gamma}} &= \sum_{t=0}^{T-1}\frac{2}{\sigma_n^2}\mathrm{Re}\{\boldsymbol{\Psi}_{\boldsymbol{\theta}}\mathbf{D}_{\boldsymbol{\Gamma}}^H[\mathbf{I} - \mathbf{A}_{\boldsymbol{\Gamma}}(\mathbf{A}_{\boldsymbol{\Gamma}}^H\mathbf{A}_{\boldsymbol{\Gamma}})^{-1}\mathbf{A}_{\boldsymbol{\Gamma}}^H] \odot [\bar{\mathbf{s}}(t)\mathbf{s}^T(t)\mathbf{A}^T\} \\
&= \frac{2T}{\sigma_n^2}\mathrm{Re}\{\boldsymbol{\Psi}_{\boldsymbol{\theta}}\mathbf{D}_{\boldsymbol{\Gamma}}^H[\mathbf{I} - \mathbf{A}_{\boldsymbol{\Gamma}}(\mathbf{A}_{\boldsymbol{\Gamma}}^H\mathbf{A}_{\boldsymbol{\Gamma}})^{-1}\mathbf{A}_{\boldsymbol{\Gamma}}^H] \odot [\frac{1}{T}\sum_{t=0}^{T-1}(\bar{\mathbf{s}}(t)\mathbf{s}^T(t)\mathbf{A}^T]\} \\
&= \frac{2T}{\sigma_n^2}\mathrm{Re}\{\boldsymbol{\Psi}_{\boldsymbol{\theta}}\mathbf{D}_{\boldsymbol{\Gamma}}^H[\mathbf{I} - \mathbf{A}_{\boldsymbol{\Gamma}}(\mathbf{A}_{\boldsymbol{\Gamma}}^H\mathbf{A}_{\boldsymbol{\Gamma}})^{-1}\mathbf{A}_{\boldsymbol{\Gamma}}^H] \odot [\mathbf{R}_s^T\mathbf{A}^T]\}.
\end{aligned} \tag{4.29}$$

Now, the full Fisher information matrix and the corresponding CRB matrix are:

$$\mathbf{F} = \begin{bmatrix} \mathbf{F}_{\boldsymbol{\theta}\boldsymbol{\theta}} & \mathbf{F}_{\boldsymbol{\theta}\boldsymbol{\gamma}} \\ \mathbf{F}_{\boldsymbol{\gamma}\boldsymbol{\theta}} & \mathbf{F}_{\boldsymbol{\gamma}\boldsymbol{\gamma}} \end{bmatrix}, \quad \mathbf{C} = \begin{bmatrix} \mathbf{C}_{\boldsymbol{\theta}\boldsymbol{\theta}} & \mathbf{C}_{\boldsymbol{\theta}\boldsymbol{\gamma}} \\ \mathbf{C}_{\boldsymbol{\gamma}\boldsymbol{\theta}} & \mathbf{C}_{\boldsymbol{\gamma}\boldsymbol{\gamma}} \end{bmatrix}, \tag{4.30}$$

where $\mathbf{F}_{\boldsymbol{\gamma}\boldsymbol{\theta}} = \mathbf{F}_{\boldsymbol{\theta}\boldsymbol{\gamma}}^H$. Since both $\mathbf{F}_{\boldsymbol{\theta}\boldsymbol{\theta}}$ and $\mathbf{F}_{\boldsymbol{\gamma}\boldsymbol{\gamma}}$ are invertible, the CRB matrices of $\boldsymbol{\theta}$ and $\boldsymbol{\gamma}$ can be obtained by applying block matrix inversion through the Schur complement:

$$\begin{aligned} \mathbf{C}_{\boldsymbol{\theta}\boldsymbol{\theta}}(\boldsymbol{\gamma}) &= \mathbf{F}_{\boldsymbol{\theta}\boldsymbol{\theta}}^{-1} + \mathbf{F}_{\boldsymbol{\theta}\boldsymbol{\theta}}^{-1}\mathbf{F}_{\boldsymbol{\theta}\boldsymbol{\gamma}}(\mathbf{F}_{\boldsymbol{\gamma}\boldsymbol{\gamma}} - \mathbf{F}_{\boldsymbol{\gamma}\boldsymbol{\theta}}\mathbf{F}_{\boldsymbol{\theta}\boldsymbol{\theta}}^{-1}\mathbf{F}_{\boldsymbol{\theta}\boldsymbol{\gamma}})^{-1}\mathbf{F}_{\boldsymbol{\gamma}\boldsymbol{\theta}}\mathbf{F}_{\boldsymbol{\theta}\boldsymbol{\theta}}^{-1}, \\ \mathbf{C}_{\boldsymbol{\gamma}\boldsymbol{\gamma}}(\boldsymbol{\theta}) &= \mathbf{F}_{\boldsymbol{\gamma}\boldsymbol{\gamma}}^{-1} + \mathbf{F}_{\boldsymbol{\gamma}\boldsymbol{\gamma}}^{-1}\mathbf{F}_{\boldsymbol{\gamma}\boldsymbol{\theta}}(\mathbf{F}_{\boldsymbol{\theta}\boldsymbol{\theta}} - \mathbf{F}_{\boldsymbol{\theta}\boldsymbol{\gamma}}\mathbf{F}_{\boldsymbol{\gamma}\boldsymbol{\gamma}}^{-1}\mathbf{F}_{\boldsymbol{\gamma}\boldsymbol{\theta}})^{-1}\mathbf{F}_{\boldsymbol{\theta}\boldsymbol{\gamma}}\mathbf{F}_{\boldsymbol{\gamma}\boldsymbol{\gamma}}^{-1}. \end{aligned} \tag{4.31}$$

In (4.31), the forms of $\mathbf{C}_{\boldsymbol{\theta}\boldsymbol{\theta}}(\boldsymbol{\gamma})$ and $\mathbf{C}_{\boldsymbol{\gamma}\boldsymbol{\gamma}}(\boldsymbol{\theta})$ are used to emphasize the dependency of one type on the other type of parameter. If one type of parameters is known, the corresponding CRB matrices are just:

$$\begin{aligned} \mathbf{C}_{\boldsymbol{\theta}\boldsymbol{\theta}} &= \mathbf{F}_{\boldsymbol{\theta}\boldsymbol{\theta}}^{-1}, \\ \mathbf{C}_{\boldsymbol{\gamma}\boldsymbol{\gamma}} &= \mathbf{F}_{\boldsymbol{\gamma}\boldsymbol{\gamma}}^{-1}. \end{aligned} \tag{4.32}$$

4.3 Conclusions

This chapter revealed that the Fisher information of $\boldsymbol{\theta}$, with the assumption that $\mathbf{s}(t)$ is deterministic, unknown and changes over time, corresponds to the mean part of the Fisher information derived from Bangs' formula. On the other hand, the Fisher information assuming $\mathbf{s}(t)$ is zero mean spatially white Gaussian corresponds to the covariance part of Bangs' formula. Assuming $\mathbf{s}(t)$ is deterministic, unknown and changing over time is beneficial since this assumption does not require a specific distribution on $\mathbf{s}(t)$, and the corresponding CRB formula explicitly illustrates the noise influence. Hence, this CRB has been chosen in this thesis. Furthermore, the Fisher of $\boldsymbol{\gamma}$, assuming $\boldsymbol{\gamma}$ is deterministic and unknown, has been derived based on the same assumption for $\mathbf{s}(t)$. Finally, the CRB matrices of $\boldsymbol{\theta}$ and $\boldsymbol{\gamma}$ for joint calibration and DoA estimation, and for the estimation of either $\boldsymbol{\theta}$ or $\boldsymbol{\gamma}$ when the other one is known, have been derived.

Cramér-Rao Bound Analysis

5

This chapter investigates the cross-impact between the DoAs and the phase errors using the CRB. Section 5.1 analyses the CRB of DoA estimation for targets with different SNR levels, under the influence of different realizations of the static phase errors and the slowly varying phase errors, aiming to illustrate the impact of unknown phase errors on the DoA estimation in stage 1 and stage 2. Section 5.2 presents the CRB of phase error estimation with different DoAs to show the impact of the unknown DoAs on the phase error estimation.

5.1 CRB of DoA estimation

To show the impact of phase errors on the DoA estimation, the CRBs of DoAs are calculated in the joint calibration and DoA estimation case, and in the calibration-aware case, under different SNR levels. For the joint estimation case, different realizations of the phase errors are applied to show the influence of phase errors on the DoA estimation. The following parameters are fixed: $M = N = 16$, $K = 2$, $T = 10$ and $D = 3$, where M and N represent the number of transmitters and receivers; K is the number of transmitter (receiver) dies; T is the number of measurements and D is the number of targets. $\mathbf{R}_s$ is assumed to be a diagonal matrix containing different strengths of the reflection coefficients:

$$\mathbf{R}_s = \begin{bmatrix} 0.4E, & 0, & 0 \\ 0, & 0.7E, & 0 \\ 0, & 0, & E \end{bmatrix}, \tag{5.1}$$

where $10 \log \frac{E}{\sigma_n^2}$ is the corresponding SNR level, and hence the strength difference between the targets is -3.98 dB (between $0.4E$ and E) and -1.55 dB (between $0.7E$ and E). Besides, the square root CRB values of the DoA estimation are in radians.

5.1.1 CRB of DoA Estimation with Static Phase Errors

In this experiment, the cross-impact between the estimation of DoAs and the static phase errors in stage 1 using the CRB is illustrated. Two realizations of DoAs for the three targets are selected: (i) $[-85.5°, -80.5°, -75.5°]^T$ and (ii) $[-5°, 0°, 5°]^T$. Case (i) is chosen since the targets around the boundaries of the Field of View (FoV) are usually difficult to estimate, and thus can provide an analysis related to the worst case. Case (ii) contains the targets from the broadside of the FoV, which is the usual case of interest. The phases of the complex inter-die phase errors are drawn from a white Gaussian distribution with standard deviation σ_{inter}, and those of the intra-die phase errors are drawn from a white Gaussian distribution with standard deviation σ_{intra}.

Different combinations of σ_{inter} and σ_{intra} are applied, and for each combination, 1000 realizations of the corresponding phase errors are calculated.

Figure 5.1 shows the results of the CRBs for the DoA estimation with targets near the boundary and around the broadside of the FoV, where $\sigma_{inter} = 10°$ and $\sigma_{intra} = 0.7°$. The shaded zone illustrates the square root CRB curves with the 1000 realizations of the phase errors. It can be observed that targets close to the boundary of the FoV result in higher CRBs than those around the broadside, and targets with lower strengths lead to higher CRBs. However, when targets are around the broadside, the corresponding CRB regions tend to be less dispersed than those when targets are close to the boundary of the FoV, and for each target, the width of the region tends to be smaller. This means that when the targets are around the broadside, the DoA estimation is more stable to target strength difference and phase errors.

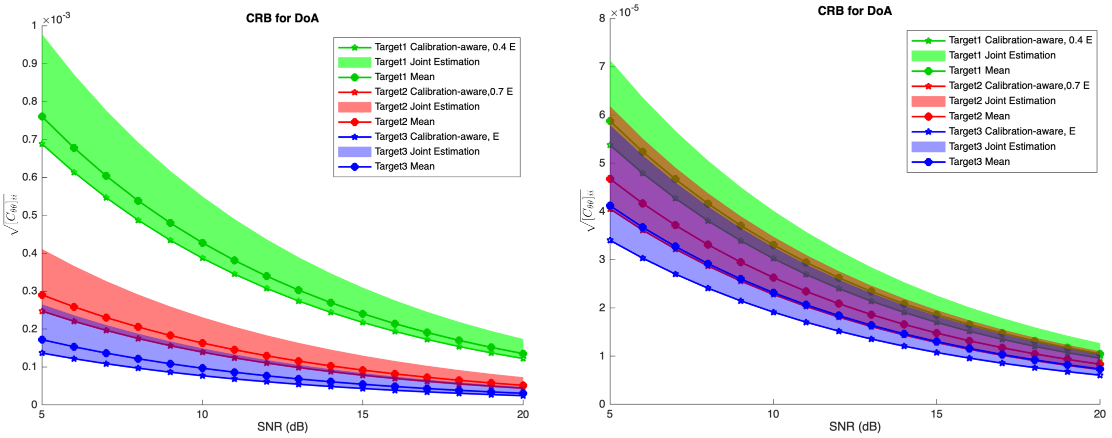

(a) Maximum and minimum zone of $\sqrt{[\mathbf{C}_{\boldsymbol{\theta\theta}}]_{ii}}(°)$ for 1000 realizations of $\boldsymbol{\gamma}$. Three targets with DoAs $-85.5°$, $-80.5°$ and $-75.5°$.

(b) Maximum and minimum zone of $\sqrt{[\mathbf{C}_{\boldsymbol{\theta\theta}}]_{ii}}(°)$ for 1000 realizations of $\boldsymbol{\gamma}$. Three targets with DoAs $-5°$, $0°$ and $5°$.

Figure 5.1: CRB for DoA estimation with static phase errors. $\sigma_{inter} = 10°$ and $\sigma_{intra} = 0.7°$.

Different values of σ_{inter} and σ_{intra} also influence the estimation of DoAs and phase errors in this stage. Hence, larger values of σ_{inter} and σ_{intra} are applied to show this influence on the CRBs.

Figure 5.2 shows the CRBs for the DoA estimation with larger σ_{inter} and σ_{intra} for the static phase errors. In Figure 5.2(a) and Figure 5.2(b), σ_{inter} increases to 10° and σ_{intra} remains 0.7°. In Figure 5.2(c) and Figure 5.2(d), σ_{intra} increases to 5° and $\sigma_{inter} = 20°$. The same observations as in Figure 5.1 can also be obtained. Moreover, by comparing Figure 5.2(a) with Figure 5.1(a), or Figure 5.2(b) with Figure 5.1(b), it can be observed that a higher value of σ_{inter} dramatically increases the width of the shaded zones, meaning an increase of the minimum variance bound for DoA estimation.

However, what is interesting is the comparison between Figure 5.2(a) and Figure 5.2(c), where the targets are close to the FoV boundary, and between Figure 5.2(b) and Figure 5.2(d), where the targets are around the broadside. The observation from the CRBs corresponding to the targets close to the FoV boundary is that a higher value of σ_{intra} causes a similar effect to that of a larger σ_{inter}. In contrast, in the case where the targets are around the broadside, the CRB zones are actually narrower when σ_{intra} becomes larger. In order to further explore this phenomenon, the impacts of the inter-die and intra-die phase errors are separated, and the results are shown in Figure 5.3. Comparing Figure 5.3(a) and Figure 5.3(b), or Figure 5.3(c) and Figure 5.3(d), it can be observed that without the other type of phase errors, increasing the standard deviation of the existing phase errors results in wider CRB zones. This is consistent with intuition. The narrower CRB zones observed in Figure 5.2(d) illustrate that the width of the CRB zones is not monotonically increasing with the increase of the two standard deviations when both types of phase error exist. This possibly means that the intra-die phase errors can offset part of the effect of the inter-die phase errors. Since σ_{inter} is much larger than σ_{intra} is the premise in this thesis, the dominant impact of phase errors on DoA estimation is from the inter-die phase errors, and possibly with a fixed σ_{inter} and $\sigma_{intra} < \sigma_{inter}$, increasing σ_{intra} from zero can increase, or decrease, the CRB zone width.

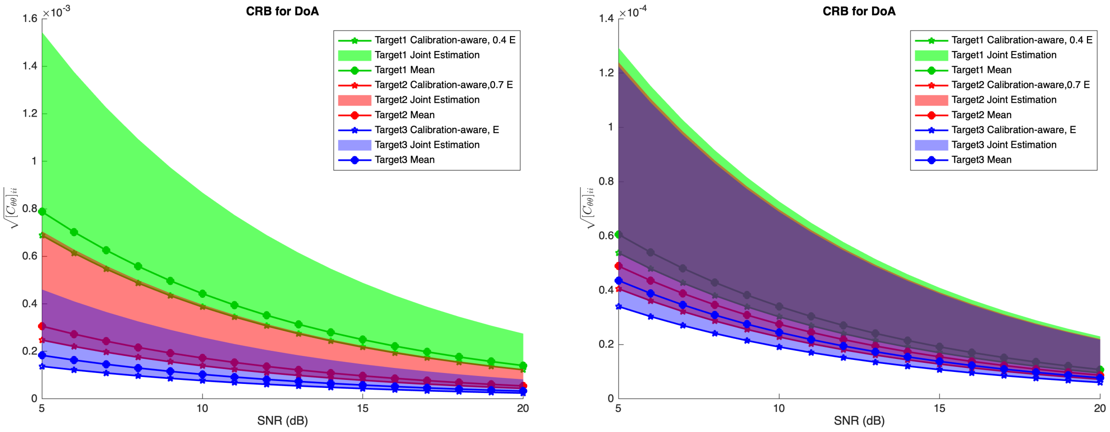

(a) Maximum and minimum zone of $\sqrt{[\mathbf{C}_{\boldsymbol{\theta\theta}}]_{ii}}$ (rad) for 1000 realizations of $\boldsymbol{\gamma}$. Three targets with DoAs $-85.5°$, $-80.5°$ and $-75.5°$. $\sigma_{inter} = 20°$ and $\sigma_{intra} = 0.7°$.

(b) Maximum and minimum zone of $\sqrt{[\mathbf{C}_{\boldsymbol{\theta\theta}}]_{ii}}$ (rad) for 1000 realizations of $\boldsymbol{\gamma}$. Three targets with DoAs $-5°$, $0°$ and $5°$. $\sigma_{inter} = 20°$ and $\sigma_{intra} = 0.7°$.

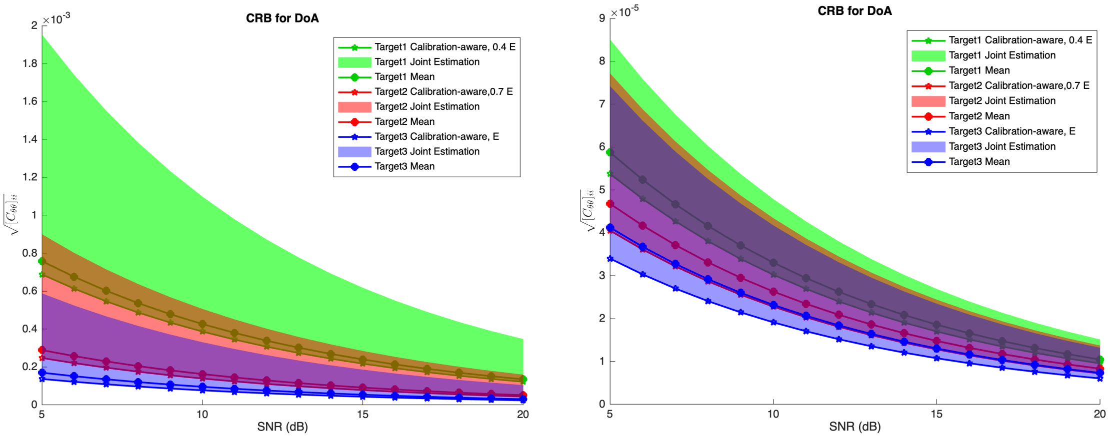

(c) Maximum and minimum zone of $\sqrt{[\mathbf{C}_{\boldsymbol{\theta\theta}}]_{ii}}$ (rad) for 1000 realizations of $\boldsymbol{\gamma}$. Three targets with DoAs $-85.5°$, $-80.5°$ and $-75.5°$. $\sigma_{inter} = 20°$ and $\sigma_{intra} = 5°$.

(d) Maximum and minimum zone of $\sqrt{[\mathbf{C}_{\boldsymbol{\theta\theta}}]_{ii}}$ (rad) for 1000 realizations of $\boldsymbol{\gamma}$. Three targets with DoAs $-5°$, $0°$ and $5°$. $\sigma_{inter} = 20°$ and $\sigma_{intra} = 5°$.

Figure 5.2: CRB for DoA estimation with larger σ_{inter} and σ_{intra} for static phase errors.

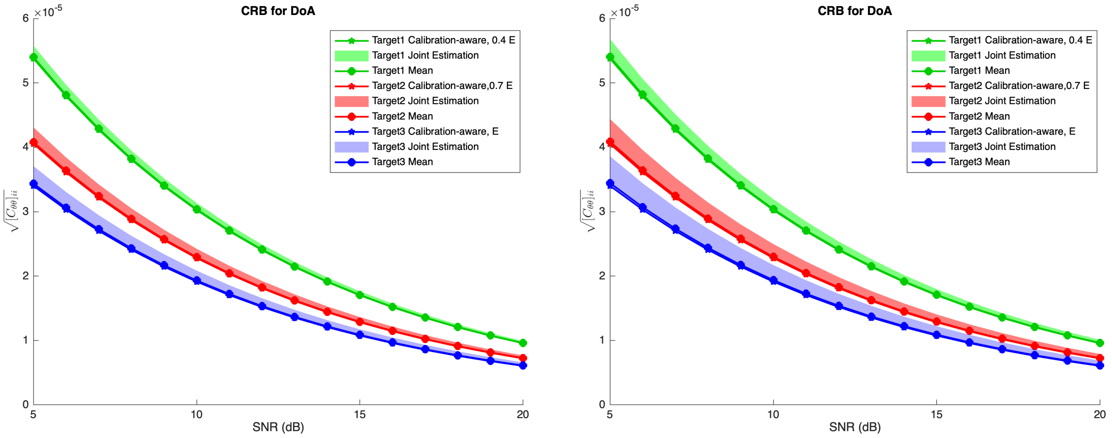

(a) Maximum and minimum zone of $\sqrt{[\mathbf{C}_{\boldsymbol{\theta}\boldsymbol{\theta}}]_{ii}}$ (rad) for 1000 realizations of $\boldsymbol{\gamma}$. $\sigma_{inter} = 0^\circ$ and $\sigma_{intra} = 0.7^\circ$.

(b) Maximum and minimum zone of $\sqrt{[\mathbf{C}_{\boldsymbol{\theta}\boldsymbol{\theta}}]_{ii}}$ (rad) for 1000 realizations of $\boldsymbol{\gamma}$. $\sigma_{inter} = 0^\circ$ and $\sigma_{intra} = 5^\circ$.

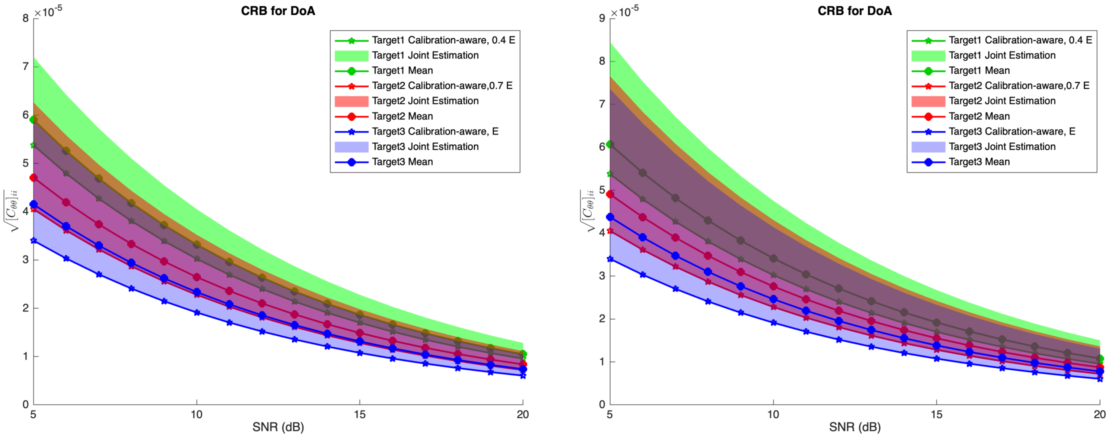

(c) Maximum and minimum zone of $\sqrt{[\mathbf{C}_{\boldsymbol{\theta}\boldsymbol{\theta}}]_{ii}}$ (rad) for 1000 realizations of $\boldsymbol{\gamma}$. $\sigma_{inter} = 10^\circ$ and $\sigma_{intra} = 0^\circ$.

(d) Maximum and minimum zone of $\sqrt{[\mathbf{C}_{\boldsymbol{\theta}\boldsymbol{\theta}}]_{ii}}$ (rad) for 1000 realizations of $\boldsymbol{\gamma}$. $\sigma_{inter} = 20^\circ$ and $\sigma_{intra} = 0^\circ$.

Figure 5.3: CRB for DoA estimation with separate impacts of different values of σ_{inter} and σ_{intra}. Three targets with DoAs -5°, 0° and 5°.

5.1.2 CRB of DoA Estimation with Slowly Varying Phase Errors

In this experiment, the cross-impact between the estimation of DoAs and the slowly varying phase errors in stage 2 using the CRB is illustrated. The DoAs are $[-5^\circ, 0^\circ, 5^\circ]^T$. 1000 simulations with 1000 different realizations of the varying phase errors are conducted. Since in this stage the phase errors change at each time index, in each simulation, a different phase error realization is applied, and the CRB for a single measurement is calculated. Because the CRB for a single measurement is also dependent on $\mathbf{s}(t)$, the calculation in both the calibration-aware and the joint estimation case shares the same 1000 realizations of $\mathbf{s}(t)$. The parameters of the slowly varying phase error model are set as follows: $\frac{\alpha}{\tau} = 0.2$, $R_0 = 1$, and $\delta = 0.05$. Figure 5.4 shows the CRBs of DoA estimation with different target strengths. The star lines represent the mean values of the calibration-aware case where the phase errors are perfectly known and compensated, corresponding to (4.32), and the shaded regions illustrate the confidence zone from the CRBs with 1000 realizations of $\boldsymbol{\gamma}$ in the joint estimation case, corresponding to (4.31). During the experiments, the curve of the mean values of the CRBs with different phase error realizations is very close to that of the calibration-aware case, compared to the relatively higher maximum values. Hence, the lower bounds of the shaded zones are defined as the minimum values of the 1000 CRB values at each SNR level, while the upper bounds are defined as the values that bound 95% of the CRB realizations. The maximum values are shown independently in Figure 5.4(b) for completion. Note here that only the mean values are shown for the calibration-aware case, as the corresponding CRB regions are too narrow to be clearly visible in the figure, especially in comparison with the joint estimation case.

It can be seen that the existence of unknown varying phase errors has a non-negligible impact on the minimum variance of the DoA estimation. In Figure 5.4(a), the curves of the minimum CRB values in the joint estimation case are not close to the mean curves of the calibration-aware case, indicating that even under the minimal impact from these varying phase error realizations, the minimum variance cannot approach the performance achieved in the calibration-aware case. Moreover, the CRBs of targets with relatively lower strengths tend to deteriorate more due to phase errors.

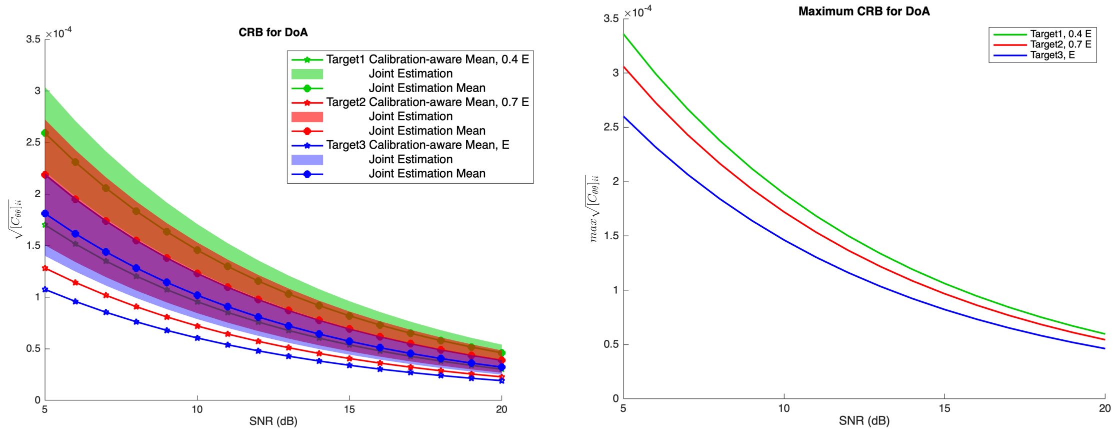

(a) Confidence zone of $\sqrt{[\mathbf{C}_{\boldsymbol{\theta\theta}}]_{ii}}$ (rad) for 1000 realizations of $\boldsymbol{\gamma}$. Three targets with DoAs $-5°$, $0°$ and $5°$.

(b) Maximum values of $\sqrt{[\mathbf{C}_{\boldsymbol{\theta\theta}}]_{ii}}$ (rad) for 1000 realizations of $\boldsymbol{\gamma}$. Three targets with DoAs $-5°$, $0°$ and $5°$.

Figure 5.4: CRB for DoAs. The green, red, and blue colors represent targets with $0.4E$, $0.7E$, and E strengths, respectively.

5.2 CRB of Phase Error Estimation

According to (4.27), the CRBs of the phase error estimation are dependent on the DoAs, both for the case where the DoAs are known and for the case where they are not known. Hence, different realizations of DoAs are chosen to analyze the impact on the phase error estimation accuracy. In detail, one target DoA is fixed to be 0°, and the other two targets are located on the two sides, with angular difference between the fixed target varying from ±5° to ±89°, with step size ±1°. The parameters are set as: $M = N = 16$, $K = 2$, $T = 10$, and $D = 3$. $\mathbf{R}_s$ is first set to be the identity matrix and then the same as in (5.1). To exclude the influence of different phase error realizations, one realization of the static phase errors is drawn with $\sigma_{inter} = 10°$ and $\sigma_{intra} = 0.7°$ and applied to all the realizations of DoAs and SNR levels.

Figure 5.5 illustrates the Root-Mean-Square (RMS) of the trace of the CRB matrices of $\boldsymbol{\gamma}$ for different DoA realizations, where the upper and lower bounds of the shaded zones are defined as the maximum and minimum values, respectively. Clearly, the DoA-aware case provides the best CRBs. Interestingly, varying DoAs have a very similar impact on the CRBs of the phase errors in both the DoA-aware and joint estimation cases. By comparing Figure 5.5(a) with Figure 5.5(b), it can be seen that the case of different target strengths results in higher CRBs.

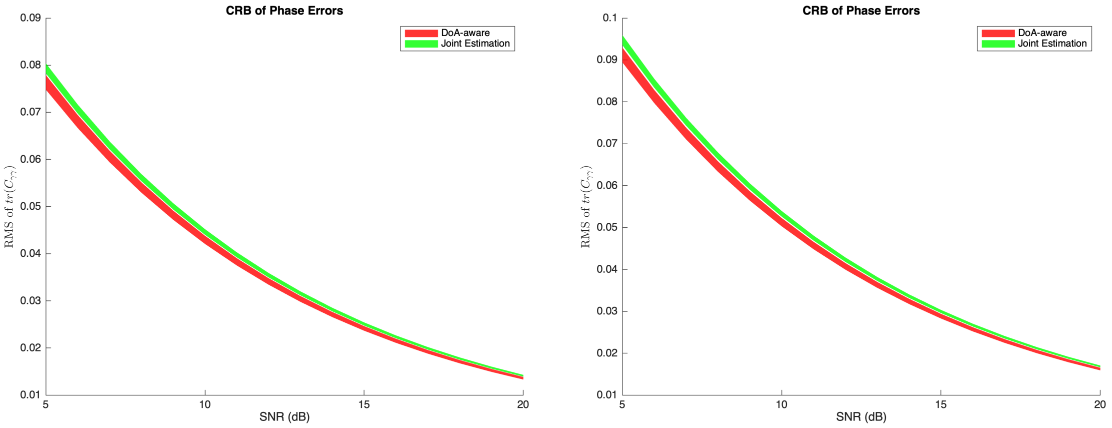

(a) Maximum and minimum zone of RMS of $\mathrm{tr}(\mathbf{C}_{\gamma\gamma})$. Three targets have equal strengths.

(b) Maximum and minimum zone of RMS of $\mathrm{tr}(\mathbf{C}_{\gamma\gamma})$. Three targets' strengths are $0.4E$, $0.7E$ and E, respectively.

Figure 5.5: CRB for phase error estimation. The green and red colors represent DoA-aware and joint estimation, respectively.

To further illustrate the influence of the angular difference on the CRB of the phase error estimation, 100 realizations of the static phase errors with $\sigma_{inter} = 10°$ and $\sigma_{intra} = 0.7°$ are drawn, and each is applied to the different realizations of the DoAs. Similar to the previous experiment, one target DoA is fixed to be 0°, and the other two targets are located on the two sides, with angular differences between the fixed target varying from ±1° to ±89°, with step size ±1°. The SNR level is fixed at $10dB$, and the strengths of the three targets are set to be the same.

Figure 5.6 shows the results of the mean and the standard deviation for the 100 realizations of the static phase errors. In Figure 5.6(a), it can be observed that when the DoAs are known, the CRBs increase significantly only when the angular differences are so large that the two targets are close to the boundaries of the FoV, otherwise, the CRBs remain almost unchanged. However, in the joint estimation case, three targets that are very close to each other also cause a slight rise in the CRBs. Furthermore, Figure 5.6(b) shows that when targets are not close to the boundaries of the FoV, the joint estimation case leads to higher standard deviations, which are almost the same as those in the DoA-aware case when the targets are close to the boundaries of the FoV. This illustrates that unknown DoAs have a larger impact on the stability of the phase error estimation.

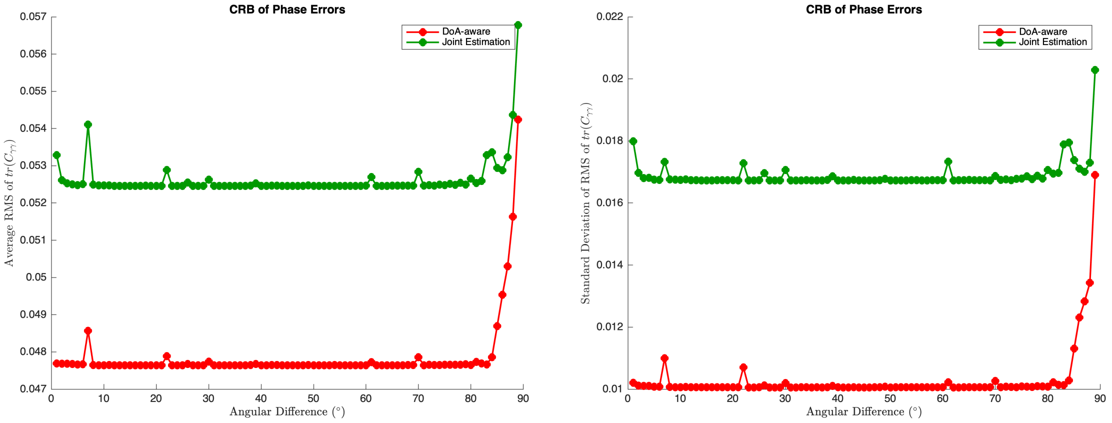

(a) Mean of the RMS of $\mathrm{tr}(\mathbf{C}_{\gamma\gamma})$.

(b) Standard Deviation of the RMS of $\mathrm{tr}(\mathbf{C}_{\gamma\gamma})$.

Figure 5.6: Mean and standard deviation of RMS of $\mathrm{tr}(\mathbf{C}_{\gamma\gamma})$ versus angular difference with 100 realizations of the static phase errors. $\sigma_{inter} = 10°$ and $\sigma_{intra} = 0.7°$.

5.3 Conclusions

In this chapter, the cross-impact between the DoA estimation and the phase error estimation has been studied, and the conclusion is that it cannot be ignored. For the DoA estimation in stage 1, the inter-die phase errors lead to a much larger increase in the CRB than the intra-die phase errors. In stage 2, with the parameters chosen for the time-varying phase error model, the slowly varying phase errors lead to an even larger increase in the CRB than the static phase errors. Besides, the CRBs corresponding to the targets close to the FoV boundary are much higher than those corresponding to the targets around the broadside, and are much more sensitive to the difference between the target SNR levels—specifically, the targets with lower SNR levels result in even higher CRBs.

The unknown DoAs also increase the CRBs of phase error estimation. Although the impact of different unknown DoA realizations is mild in general, the phase error estimation becomes less stable for different target locations, and the DoAs of the targets close to the FoV boundaries actually increase the CRBs dramatically.

6 Conclusions and Future Work

6.1 Conclusions

This thesis investigated the joint sensor calibration and DoA estimation problem in the context of modular-design automotive radar systems from two perspectives: (i) proposing an approach to calibrate sensors and estimate DoAs, and (ii) Cramér-Rao bound analysis of the cross-impact between phase errors and DoAs.

An approach consisting of two steps was proposed to solve the joint estimation problem: (i) the die structure-based convex optimization method and (ii) the PAST-based alternating update. Accordingly, the entire joint sensor calibration and DoA estimation scenario was divided into two stages: (i) static stage and (ii) varying stage. During the first stage, it was assumed that the phase errors are static, and a convex optimization problem based on the sparsity assumption of the targets was derived to estimate the initial phase errors and DoAs [12]. To solve the system of equations in this convex optimization approach, a die structure-based phase error model was proposed to focus on the inter-die phase errors while ignoring the intra-die phase errors. The experiments showed that this convex optimization approach with the die structure-based phase error model can accurately estimate DoAs and reasonable initial phase errors without requiring a large number of measurements or high SNR levels.

An alternating update algorithm was proposed for the second stage, where the phase errors are time-varying. This approach updates the DoA and phase error estimates in each iteration based on the initial estimates from stage 1 by optimzing the MUSIC pseudo-spectrum. The method utilizes a subspace tracking technique called PAST [18, 19] to avoid the high computational cost related to the EVD. The experiments demonstrated that this approach can track varying phase errors with lower computational cost and is robust to variations in the phase errors.

Monte-Carlo simulations of the beampatterns from the calibrated array in both steps were conducted. The results demonstrated the effectiveness of the proposed two-step approach in suppressing the peaking sidelobes while maintaining angular resolution.

A dynamic range test was also conducted on the proposed two-step approach, where the two targets are close to each other with a dramatic difference in their SNR levels. The results not only illustrated that the proposed approach can indeed improve the estimation accuracy and stability, but also suggested the applicability of the PAST-based and the EVD-based alternating update approach in different conditions: the EVD-based method is suitable for the situation where stage 2 is of shorter duration, i.e., within 100 radar cycles under the experimental conditions, while the PAST-based one is more suitable for long-term tracking.

What followed was the CRB derivation and analysis. The CRB has different expressions under different assumptions. In this thesis, assuming the phase errors are known, the Fisher information for the DoAs was derived according to Bangs' formula [20]. The derivation mathematically showed the relation between two different assumptions: (i) the reflection coefficients have zero variance and a varying mean, and (ii) the reflection coefficients are zero mean spatially white Gaussian. The first assumption corresponds to the mean information part of the Fisher information derived from Bangs' formula, whereas the second assumption corresponds to the covariance part. The first assumption was chosen for further analysis because it does not impose any constraint on the distribution of the reflection coefficients. Next, the CRB of the DoAs and phase errors, assuming both of them have zero variance and varying mean, was derived.

Monte-Carlo simulations for the CRBs of both the DoA and phase error estimates were conducted in order to analyze the cross-impact. On one hand, the simulations showed that the phase errors have a non-negligible negative impact on DoA estimation, whereas on the other hand, unknown DoAs disturb the best achievable performance of the phase error estimation.

6.2 Future Work

Future work spans a wide range of directions. Among these, the following aspects emerged as particularly interesting during the implementation of this thesis. Although they have not yet been addressed, they offer promising opportunities for further exploration:

- **Investigating method-dependent performance indicators**

  This thesis investigates the cross-impact between the phase error and DoA estimation using the CRB since it does not depend on a specific estimation method. But there is no doubt that method-dependent performance indicators are also useful, e.g., the MUSIC algorithm performance for DoA estimation. It is possible to consider the phase errors as perturbations of the signal subspace, so that the phase error impact can be related to the eigenvalues and eigenvectors. Similarly, taking the subspace-based phase error estimation method as an example, evaluating the impact of the signal subspace related to targets with different angular separations or SNR levels on the phase error estimation can provide more insights. These potential method-dependent indicators provide new perspectives for quantifying and analyzing the cross-impact between the phase error and DoA estimation.

- **Incorporating mutual coupling and gain errors**

  The current work considers no mutual coupling, i.e., the phase error matrix $\mathbf{\Gamma}$ is diagonal. However, in reality, each array element receives not only its primary voltage induced by the incident radiation but also additional contributions from reflected radiation and surface currents originating from neighboring elements, which makes $\mathbf{\Gamma}$ no longer a diagonal matrix. Besides, although it is possible to tackle the gain errors by built-in hardware systems, an algorithm involving blind calibration of both gain and phase errors can reduce this hardware cost. These bring new perspectives and challenges to the current approach.

- **Incorporating real effects into the varying error model**

The current model for the slowly varying phase errors is based on an autocorrelation function that decays over time. Still, it does not explicitly incorporate the temperature variations and aging effects. In reality, the phase errors are caused mainly by factors such as temperature variations and aging effects, and such correlation with these factors is usually more complex and, likely, a more precise and rigorous mathematical model for these factors exists. Incorporating these effects makes the proposed approach more persuasive.

- **Incorporating moving targets with realistic mobility models**

  The current work focuses on antenna calibration and DoA estimation with static targets. In reality, most targets are moving, while time-varying effects, i.e., temperature variations and aging effects, also degrade system performance. Incorporating DoA estimation for moving targets provides the possibility for a wider range of practical scenarios. Besides, similar to the aforementioned phase errors, there is no doubt that an accurate model for DoAs of moving targets is preferable. Simulators from professional resources are good choices.

- **Studying two-dimensional (2D) antenna arrays**

  In this thesis, azimuth is the only focus. In reality, however, both azimuth and elevation are of interest. As a natural extension, future research will investigate two-dimensional (2D) antenna arrays, which provide enhanced spatial coverage and allow for more degrees of freedom in DoA estimation.

Bibliography

[1] J. Capon, "High-resolution frequency-wavenumber spectrum analysis," *Proceedings of the IEEE*, vol. 57, no. 8, pp. 1408–1418, 1969.

[2] R. Roy and T. Kailath, "ESPRIT-estimation of signal parameters via rotational invariance techniques," *IEEE Transactions on Acoustics, Speech, and Signal Processing*, vol. 37, no. 7, pp. 984–995, 1989.

[3] H. L. Van Trees, *Optimum array processing: Part IV of detection, estimation, and modulation theory.* John Wiley & Sons, 2002.

[4] Z. Jaafer, S. Goli, and A. S. Elameer, "Performance Analysis of Beam scan, MIN-NORM, Music and Mvdr DOA Estimation Algorithms," in *2018 International Conference on Engineering Technology and their Applications (IICETA)*, 2018, pp. 72–76.

[5] O. A. Oumar, M. F. Siyau, and T. P. Sattar, "Comparison between MUSIC and ESPRIT direction of arrival estimation algorithms for wireless communication systems," in *The First International Conference on Future Generation Communication Technologies*, 2012, pp. 99–103.

[6] A. Swindlehurst and T. Kailath, "A performance analysis of subspace-based methods in the presence of model errors. I. The MUSIC algorithm," *IEEE Transactions on Signal Processing*, vol. 40, no. 7, pp. 1758–1774, 1992.

[7] A. Paulraj and T. Kailath, "Direction of arrival estimation by eigenstructure methods with unknown sensor gain and phase," in *ICASSP '85. IEEE International Conference on Acoustics, Speech, and Signal Processing*, vol. 10, 1985, pp. 640–643.

[8] M. Wylie, S. Roy, and H. Messer, "Joint DOA estimation and phase calibration of linear equispaced (LES) arrays," *IEEE Transactions on Signal Processing*, vol. 42, no. 12, pp. 3449–3459, 1994.

[9] Y. Li and M. Er, "Theoretical analyses of gain and phase error calibration with optimal implementation for linear equispaced array," *IEEE Transactions on Signal Processing*, vol. 54, no. 2, pp. 712–723, 2006.

[10] B. Friedlander and A. Weiss, "Eigenstructure methods for direction finding with sensor gain and phase uncertainties," in *ICASSP-88., International Conference on Acoustics, Speech, and Signal Processing*, 1988, pp. 2681–2684 vol.5.

[11] S. J. Wijnholds and A.-J. van der Veen, "Multisource self-calibration for sensor arrays," *IEEE Transactions on Signal Processing*, vol. 57, no. 9, pp. 3512–3522, 2009.

[12] K. N. Ramamohan, S. P. Chepuri, D. F. Comesana, and G. Leus, "Self Calibration of Scalar and Vector Sensor Arrays," *arXiv preprint arXiv:2104.02561*, 2021.

[13] K. Zhang, "Optimal Sensor Placement for Calibration-Involved Radio Astronomy Imaging Applications," https://resolver.tudelft.nl/uuid:6ab4964d-4215-433f-81d1-60417eab369a, 2020, master's Thesis, TU Delft.

[14] P. Stoica, B. Ottersten, M. Viberg, and R. Moses, "Maximum likelihood array processing for stochastic coherent sources," *IEEE Transactions on Signal Processing*, vol. 44, no. 1, pp. 96–105, 1996.

[15] C. A. Kokke, M. Coutino, L. Anitori, R. Heusdens, and G. Leus, "Sensor Selection for Angle of Arrival Estimation Based on the Two-Target Cramer-Rao Bound," *in ICASSP 2023 - 2023 IEEE International Conference on Acoustics, Speech and Signal Processing (ICASSP)*, 2023.

[16] C. A. Kokke, M. Coutino, R. Heusdens, and G. Leus, "Array Design Based on the Worst-Case Cramér-Rao Bound to Account for Multiple Targets," in *2023 57th Asilomar Conference on Signals, Systems, and Computers*, 2023.

[17] P. Stoica and A. Nehorai, "MUSIC, maximum likelihood, and Cramer-Rao bound," *IEEE Transactions on Acoustics, Speech, and Signal Processing*, vol. 37, no. 5, pp. 720–741, 1989.

[18] B. Yang, "Subspace tracking based on the projection approach and the recursive least squares method," in *1993 IEEE International Conference on Acoustics, Speech, and Signal Processing*, vol. 4, 1993, pp. 145–148 vol.4.

[19] ——, "Projection approximation subspace tracking," *IEEE Transactions on Signal Processing*, vol. 43, no. 1, pp. 95–107, 1995.

[20] W. J. Bangs, *Array processing with generalized beam-formers.* Yale University, 1971.

[21] H. Hung and M. Kaveh, "On the statistical sufficiency of the coherently averaged covariance matrix for the estimation of the parameters of wideband sources," in *ICASSP '87. IEEE International Conference on Acoustics, Speech, and Signal Processing*, 1987.

[22] H. L. Van Trees, *Optimum array processing: Part IV of detection, estimation, and modulation theory.* John Wiley & Sons, 2002.